# REPORT DOCUMENTATION PAGE

*Form Approved*
*OMB No. 0704-0188*



**PLEASE DO NOT RETURN YOUR FORM TO THE ABOVE ORGANIZATION.**

| 1. REPORT DATE *(DD-MM-YYYY)* | 2. REPORT TYPE | 3. DATES COVERED *(From - To)* |
|---|---|---|
| | FINAL REPORT | 01 SEP 2005 - 28 FEB 2007 |

**4. TITLE AND SUBTITLE**
(DARPA) LOGIC NANOCELLS WITHIN 3-TERMINAL ORDERED ARRAYS

**5a. CONTRACT NUMBER**

**5b. GRANT NUMBER**
FA9550-05-1-0476

**5c. PROGRAM ELEMENT NUMBER**
62716E

**6. AUTHOR(S)**
DR TOUR

**5d. PROJECT NUMBER**
U029/00

**5e. TASK NUMBER**

**5f. WORK UNIT NUMBER**

**7. PERFORMING ORGANIZATION NAME(S) AND ADDRESS(ES)**
WILLIAM MARSH RICE UNIVERSITY
6100 MAIN STREET
HOUSTON TX 77005

**8. PERFORMING ORGANIZATION REPORT NUMBER**

**9. SPONSORING/MONITORING AGENCY NAME(S) AND ADDRESS(ES)**
AF OFFICE OF SCIENTIFIC RESEARCH
875 NORTH RANDOLPH STREET ROOM 3112
ARLINGTON VA 22203
DR ANNE MATSUURA

**10. SPONSOR/MONITOR'S ACRONYM(S)**

**11. SPONSOR/MONITOR'S REPORT NUMBER(S)**

**12. DISTRIBUTION/AVAILABILITY STATEMENT**
DISTRIBUTION STATEMEN A: UNLIMITED

AFRL-SR-AR-TR-07-0494

**13. SUPPLEMENTARY NOTES**

**14. ABSTRACT**
ON SEPARATE SHEET



**15. SUBJECT TERMS**

| 16. SECURITY CLASSIFICATION OF: | | | 17. LIMITATION OF ABSTRACT | 18. NUMBER OF PAGES | 19a. NAME OF RESPONSIBLE PERSON |
|---|---|---|---|---|---|
| a. REPORT | b. ABSTRACT | c. THIS PAGE | | | 19b. TELEPHONE NUMBER *(Include area code)* |
| | | | | | |

We have controllably modulated the drain current *(ID)* and threshold voltage ***(V-$_1$-)*** in pseudo metal-oxide-semiconductor field-effect transistors (MOSFETs) by grafting a monolayer of molecules atop oxide-free H-passivated silicon surfaces. An electronically controlled series of molecules, from strong it-electron donors to strong it-electron acceptors, was covalently attached onto the channel region of the transistors. The device conductance was thus systematically tuned in accordance with the electron-donating ability of the grafted molecules, which is attributed to the charge transfer between the device channel and the molecules. This surface grafting protocol might serve as a useful method for controlling electronic characteristics in small silicon devices at future technology nodes.

A series of transition metal coordination complexes designed to assemble on gold surfaces was synthesized, their electronic structure and transitions analyzed, and their magnetic properties studied. By taking advantage of recently developed thiocyanate assembly protocols, these molecules were then assembled onto a gold surface, without the need for an inert atmosphere, to give a loosely packed monolayer. This molecular assembly was designed for and used in single molecule transistors (SMT5).

Thiocyanate assembly is shown to be an effective method for assembling thiolate structures on platinum, silver, and gold. The assemblies were studied by infrared reflection spectroscopy and X-ray photoelectron spectroscopy (XPS). Two cyanide species were identified on the surfaces: the first corresponding to adsorbed cyanide and the second to a form commonly seen as an intermediate during cyanide etching of metals. The presence of the second species supports the theory that cyanide is leaving the surface as M(CN)X, resulting in a thiolate monolayer. Comparison of thiocyanate assemblies on evaporated gold and silver to those on template-stripped gold demonstrates the integral role of surface morphology in the expulsion of $(CN)_{ads}$ from the surface of the metals.

## Contract Information

| | |
|---|---|
| Contract Number | FA9550-05-1-0476 |
| Title of Research | Logic NanoCells Within 3-Terminal Ordered Arrays |
| Principal Investigator | James M. Tour |
| Organization | William Marsh Rice University |

## Technical Section

### *Technical Objectives*

For this BAA 03-12 on MoleComputing, we proposed an architecture wherein we interfaced moleware (molecular hardware) technology into 3-terminal MOSFET-like structures that show gain and isolation. In that way, we would permit the semiconductor to "do the heavy lifting" by carrying the current, and the molecules would serve as a surface carrier to modulate the transconductance via a gate. Due to the intense funding cuts that were enacted between the original submission of this proposal and this revised version, this MOSFET/molecule study will take precedence in Phase 1, and then they will be incorporated into the NanoCell during the later Phases of the research.

### *Technical Approach*

Our overall technical approach to this project consisted of the following elements: (a) A rich set of chemistries available to form the channel of a moleware device, and considerable insight and experience into the functionality of the device and these chemistries. We have in-depth experience in attachment chemistries to both metals and semiconductors. Note that worldwide, more groups are experimenting with the chemical basis set developed in our program, than any other chemical basis set; (b) A complete numerical tool-kit for modeling of large molecular-organic systems from first-principles. Numerical simulation is essential for device fine-tuning due to the complexity of the overall structure. The same situation is true in the MOSFET world; physics-based models permit high-level understanding and are useful in device simulation, while numerical models are used for detailed devices; (c) a simple concept for building 3-terminal devices. Note this is a Field Effect device (like a MOSFET); (d) approaches to further define molecular signatures on molecules bound to metals and to semiconductors; (e)interface of molecules to MOSFETs via a diverse set of chemistries in an effort to exploit the best of both architectures and thereby be poised for the nanoscale solid state revolution wherein the devices have a high surface area; molecules doping the surface for controlling the transconductance.

***Progress Statement Summary—Final Technical Report***

We have controllably modulated the drain current ($I_D$) and threshold voltage ($V_T$) in pseudo metal-oxide-semiconductor field-effect transistors (MOSFETs) by grafting a monolayer of molecules atop oxide-free H-passivated silicon surfaces. An electronically controlled series of molecules, from strong $\pi$-electron donors to strong $\pi$-electron acceptors, was covalently attached onto the channel region of the transistors. The device conductance was thus systematically tuned in accordance with the electron-donating ability of the grafted molecules, which is attributed to the charge transfer between the device channel and the molecules. This surface grafting protocol might serve as a useful method for controlling electronic characteristics in small silicon devices at future technology nodes.

A series of transition metal coordination complexes designed to assemble on gold surfaces was synthesized, their electronic structure and transitions analyzed, and their magnetic properties studied. By taking advantage of recently developed thiocyanate assembly protocols, these molecules were then assembled onto a gold surface, without the need for an inert atmosphere, to give a loosely packed monolayer. This molecular assembly was designed for and used in single molecule transistors (SMTs).

Thiocyanate assembly is shown to be an effective method for assembling thiolate structures on platinum, silver, and gold. The assemblies were studied by infrared reflection spectroscopy and X-ray photoelectron spectroscopy (XPS). Two cyanide species were identified on the surfaces: the first corresponding to adsorbed cyanide and the second to a form commonly seen as an intermediate during cyanide etching of metals. The presence of the second species supports the theory that cyanide is leaving the surface as $M(CN)_x$, resulting in a thiolate monolayer. Comparison of thiocyanate assemblies on evaporated gold and silver to those on template-stripped gold demonstrates the integral role of surface morphology in the expulsion of $(CN)_{ads}$ from the surface of the metals.

***Progress—Final Technical Report***

## Controlled Modulation of Conductance in Silicon Devices by Molecular Monolayers

### Introduction

Although a number of alternatives to silicon-based materials have been proposed,[1-3] silicon remains the stalwart of the electronics industry. Generally, the behavior of silicon is controlled by changing the composition of the active region by impurity doping;[4] while changing the surface (interface) states is also possible.[5-8] As scaling to the sub-20 nm-size region is pursued, routine impurity doping becomes problematic due to its resultant uncertainty of distribution.[9,10] Provided back-end processing of future devices could be held to temperatures that are molecularly permissive (300-350°C)[11] and taking advantage of the dramatic increase in the surface-area-to-volume-ratios of small

features, it is attractive to seek controllable modulation of device performance through surface modifications.

Several techniques have been used to covalently attach molecules directly onto silicon surfaces.[12-15] The Si-C bond formed using these methods is both thermodynamically and kinetically stable due to its high bond strength (3.5 eV) and low polarity.[15,16] The majority of research in this area has focused on the grafting methods or the influence on the surface (or interface) properties of bulk semiconductors. Related work is in the use of semiconductor devices as sensors, specifically the chemically sensitive field-effect transistors (CHEMFETs)[17-20] and the molecularly controlled semiconductor resistor based on transistors.[21-23] In these devices, however, the chemicals or molecules are usually attached on the gate metal and/or insulator layer of a field-effect transistor (FET), between source and drain of an ungated FET, or on the surface metal of Schottky diodes. So far little research has been conducted showing controlled modulation of semiconductor devices by grafting molecular layers onto oxide-free active device areas, and particularly via silicon—$sp^2$-hybridized-carbon bonds. Since there is no intervening oxide between the -rich molecules and the silicon, sequentially tuned molecular-structure changes can predictably regulate the device performances over a wide range. Furthermore, gating a FET can increase the sensitivity of sensors to adsorbed chemicals.[21] In this contribution, an electronically controlled series of molecules, from strong -electron donors to strong -electron acceptors, were prepared and systematically covalently attached as molecular monolayers onto the channel region of pseudo-MOSFETs (back gated), and the device modulation was studied.

## Experimental Section

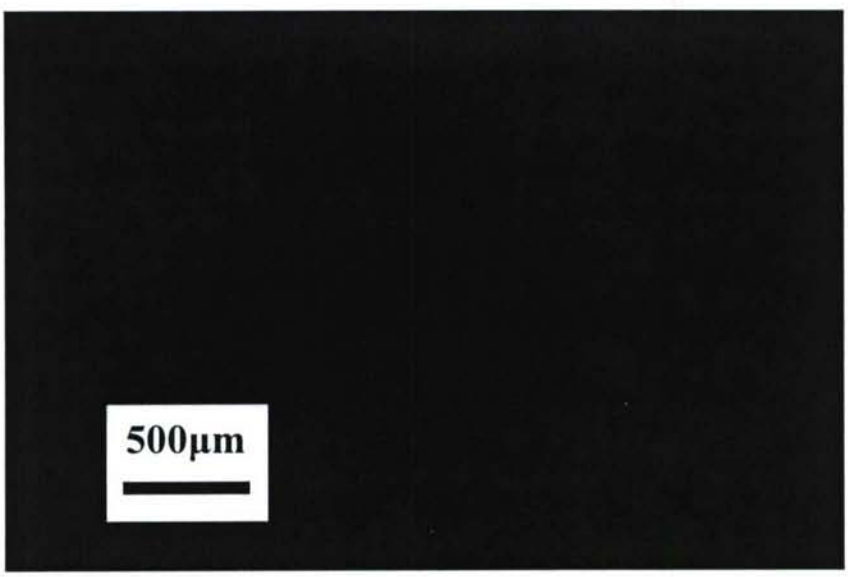

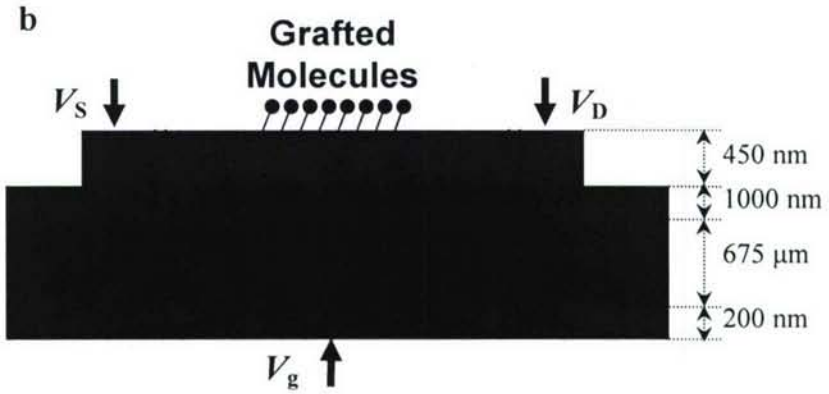


**Figure 1.** (**a**) An optical micrograph of some devices on one chip. Boxed regions indicate the source and drain, between which sits the channel. The data shown in this contribution were collected with Row 0, for which both the length and width of the channel are 100 μm and the active area for molecular assembly is 110 × 110 $\mu m^2$. (**b**) Schematic side-view representation (not to scale) of the device. The molecules were grafted between source and drain electrodes. $V_S$, $V_D$, and $V_g$ refer to the bias applied on the source, drain, and gate, respectively.

**Device fabrication.** The pseudo-MOSFET devices were fabricated using a silicon-on insulator (SOI) wafer (Figure 1). The handle wafer was p-Si (boron doped, <100>, 14-22 Ω·cm, 675 μm thick). The device layer was the nearly intrinsic p-Si (boron doped, <100>, > 2000 Ω·cm, 450 nm thick). The BOX thickness was 1000 nm. The source and drain electrodes (80 × 80 $\mu m^2$) were highly doped with boron at a level of about $10^{20}$ $cm^{-3}$ (~$10^{-3}$ Ω·cm) and about 130 nm deep to get an ohmic contact. Thus the isolated devices had $p^{++}$ junctions. To avoid destroying the grafted molecules and interfering with their influence, we used this simple back-gating design instead of a more complicated and potentially damaging top-gate fabrication. The back contact of the structure was achieved by sputter-coating a 200 nm Au layer.

**Molecular grafting.** Compounds **1**, **2** and **3** were synthesized according to literature methods.[24-26] The synthesis of **4** is given in the Supporting Information. The molecules **1**-**4** were directly grafted onto the active area in the channel region of the device using the method reported previously.[13] Before the molecular grafting, the devices were etched in an Ar purged buffered oxide etch (BOE, J. T. Baker, 10:1, CMOS grade) for 5 min to remove the oxide layer and form the H-passivated silicon surface. The grafting process was carried out by exposing the freshly etched samples to a 0.5 mM solution of the diazonium salt (**1**-**4**) in anhydrous acetonitrile ($CH_3CN$) in the dark under an inert atmosphere. The grafting time depends on the molecule that was used, and that was carefully calibrated. Before the grafting of molecules (**1**-**4**) onto the channel, we first studied the assembly protocol on a p-Si wafer (with the orientation of both <100> and <111>) so as to ensure that a molecular monolayer (not a multilayer) was being formed (see Supporting Information). The grafting time was 5 h for compound **1**, 45 min for **2** and **3**, and 2 h for **4**. Molecular layer thicknesses were monitored using a single wavelength (632.8 nm laser) Gaertner Stokes ellipsometer with an incident angle of 70°. X-ray photoelectron spectroscopy (XPS, PHI 5700 XPS/ESCA system) was used to

ensure the molecules were directly grafted on the silicon surface. The ellipsometric and XPS results are given in the Supporting Information. After the molecular grafting, the samples were rinsed thoroughly with $CH_3CN$ to remove the residual diazonium salt and the physisorbed materials, and then dried with an $N_2$ flow.

**Device testing.** The samples were tested with a probe station (Desert Cryogenics TT-prober system) under a vacuum < $5 \times 10^{-6}$ torr. The metal tips (ZN50R-25-BeCu or ZN50R-25-W, Desert Cryogenics) were softly probed directly onto the source/drain contacts using micron manipulators. The DC $I(V)$ data were collected by using a semiconductor parameter analyzer (Agilent 4155C). First, all the devices were tested immediately after the BOE etching and before the molecular grafting. To get freshly cleaned surface for molecular grafting, the devices were then subjected to a second short etching with BOE (30-60 s) and were transferred into the glove box for grafting. A second DC $I(V)$ measurement was done after the grafting was completed. Devices with no molecules (H-passivated surface) were prepared and tested as the control samples. To study the influences from the second etching on the device performance, the control samples experienced the same treatment history as the devices under test, but without the molecular attachment, and the DC $I(V)$ measurements were carried out after each BOE etching. Both molecular grafting and testing were done at room temperature.

## Results and Discussion

Although not the optimal design for large-scale fabrication, the pseudo-MOSFET serves as a proof-of-concept device for performance modulation by monolayer molecular grafting, obviating more rigorous designs for grafting within top-gated configurations. Note the pseudo-MOSFET structure can produce pure MOSFET-like characteristics,[27] which is confirmed by our experimental results. In a pseudo-MOSFET, the bulk p-Si substrate (handle) acts as a gate terminal and is biased ($V_g$), through the Au back contact, to induce a conduction channel at the upper interface of the buried oxide (BOX). This BOX is used as a gate dielectric layer. As in our case, an accumulation channel (p-channel) was activated when both the gate ($V_g > V_T$) and drain were negatively biased. Since the transistor body is the nearly intrinsic p-Si layer (> 2000 Ω·cm and 450 nm thick), the channel is assumed to be completely accumulated. The source and drain areas were highly doped ($10^{20}$ $cm^{-3}$) to ensure ohmic contact when metal tips were brought to probe the source and drain electrodes. Since the doping levels of the junctions are much greater than that of the channel, the influence of the source and drain parasitic series resistances were negligible. The molecules (Figure 2a) were grafted in the channel region between the drain and source electrodes. The diazonium portion of the molecule is lost resulting in a direct aryl-silicon bond (Figure 2b), as we have described previously.[13]

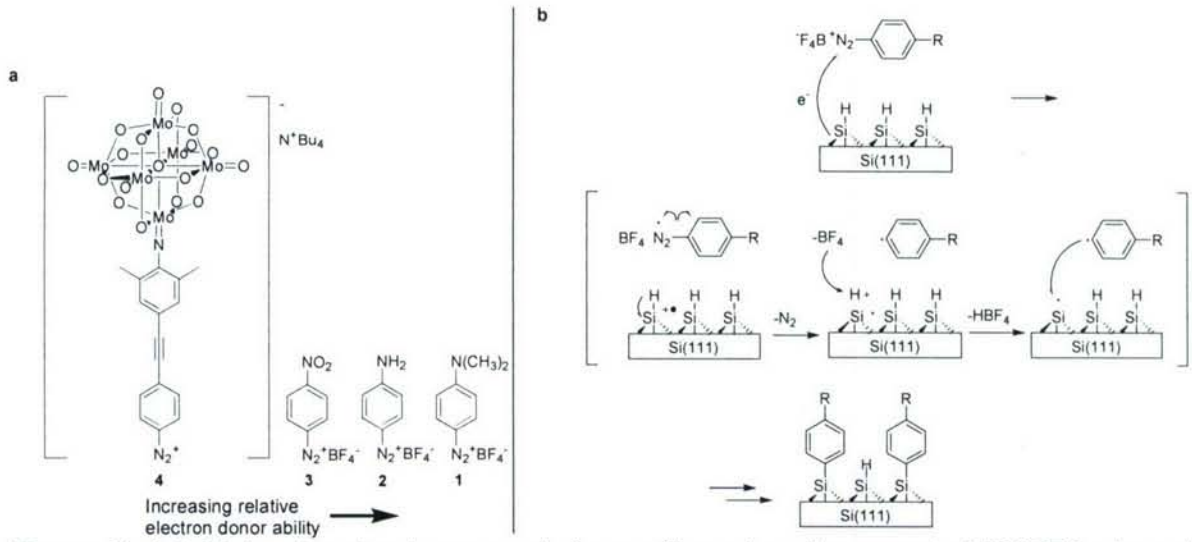


**Figure 2.** (**a**) Molecular structures used for grafting atop the pseudo-MOSFET channel. Structures of the starting molecules **1**-**4** used in the present contribution where **1** is the most electron rich system due to the dimethylamino substituent, **2** is slightly lower in its electron donation capability, followed by **3,** and then finally **4** bears an extremely electropositive polymolybdate. (**b**) The mechanism of the reaction of H-passivated Si with aryldiazonium salts is illustrated.[13] In this case, the R-group represents the *para*-moiety on the grafted aryl ring.

Figure 3 shows the typical transfer characteristics of the devices under test before and after the grafting of molecular monolayers. It is assumed there are no short- or narrow-channel effects since both the length and width of the device channel used here were 100 μm. For compounds **1**-**3**, the drain current under the same gate bias decreased after the molecular grafting. The amplitude of this decrease is in the order of **1** > **2** > **3**. But $I_D$ increased slightly after the grafting of **4**. The hystereses observed in the $I_D$-$V_g$ curves are very similar in amplitude and shape before and after the molecular attachment (Figure 3). Therefore these hysteretic effects are caused by the device itself, not by the molecular grafting.

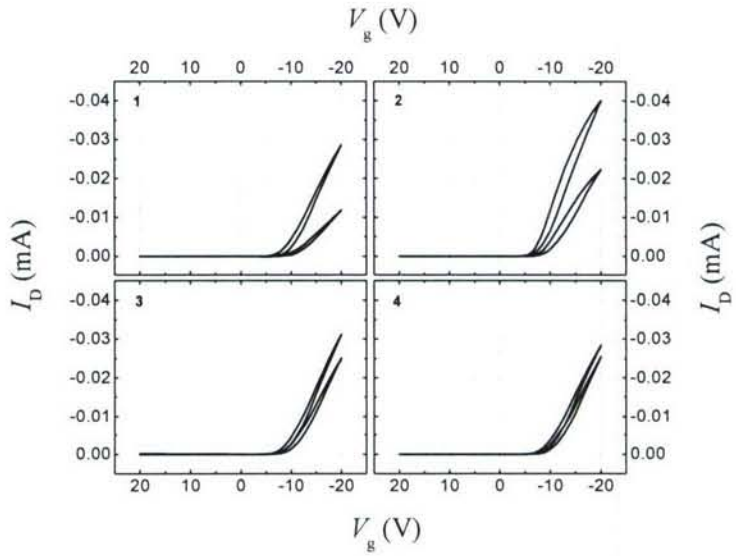


**Figure 3.** Transfer characteristics of the devices under test before (black) and after (red) the grafting of different molecular monolayers. The numbers (1, 2, 3 and 4) in the illustrations correspond to the compounds **1**-**4**, respectively. Data shown here were collected under -5 V of $V_D$ and is the average value for 14 devices from Row 0 on one chip, as described in Figure 1a, and they are characteristic of the hystereses observed in all the devices. The gate bias was scanned first from +20 V to -20 V (forward) and then back from -20 V to +20 V.

$V_T$ can be extracted based on the measurement of $I_D$, which represents the onset of significant drain current and is a fundamental parameter for MOSFET characterization and modeling. The $V_T$ values shown here were determined from the $V_g$ axis intercept of the $I_{D,Sat}^{0.5}$-$V_g$ characteristics linearly extrapolated,[28-30] as shown in Figure 4a (also see Supporting Information). Figure 4b shows the representative change in $V_T$ ($\Delta V_T$) of the devices under test before and after the grafting of molecular monolayers. It is seen from Figure 4b that the $V_T$ became more negative (usually about 1 ~ 2 V) after grafting **1**, **2** and **3** while less negative for **4**, relative to the control which was the Si-H surface before molecular grafting. Though there are slight differences between the values of $\Delta V_T$ when $V_T$ was extracted from the forward and back scans (Figure 4b) due to the inherent hysteretic nature of the devices themselves (Figure 3), the same trend in the change of $V_T$ was observed. The control samples experienced the same treatment history as the devices under test, but had no molecules grafted on them, only the hydrogen passivation remained. For control samples, the $V_T$ changed slightly (typically ≤ 0.3 V) from the first to the second etching. This supports our assertion that the $V_T$ change in the devices under test is not caused by the etching but by the molecular grafting on the channel region which tracks directly with the electron donor ability of the molecules.

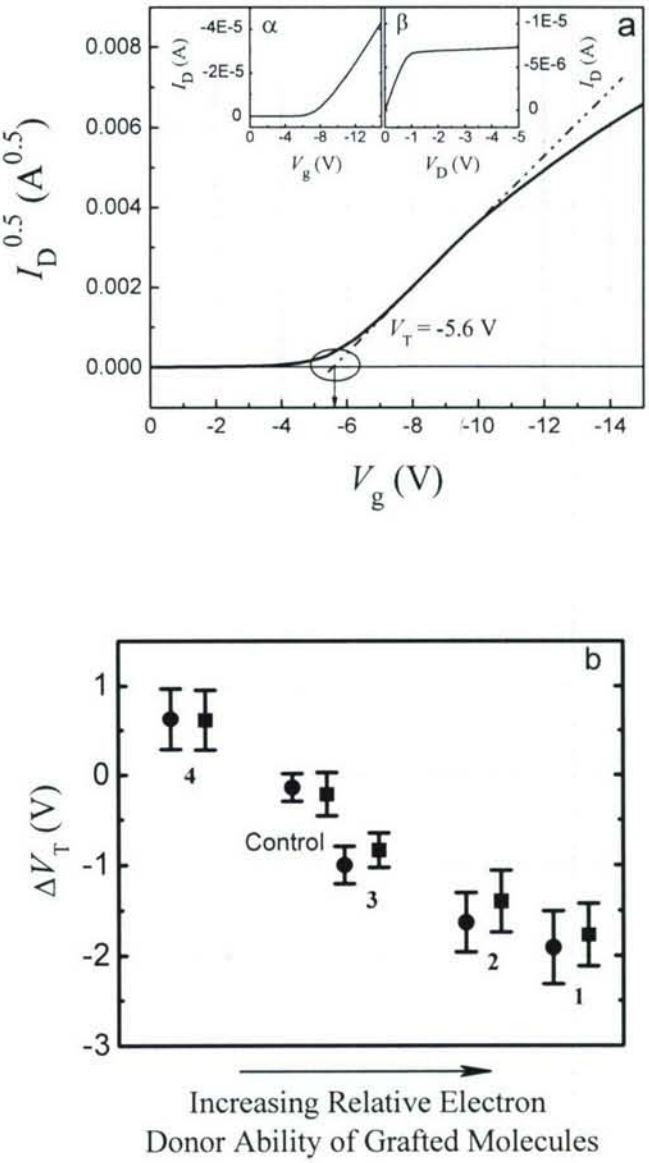


**Figure 4.** Electrical output results of the pseudo-MOSFET devices. (**a**) Extrapolation method for $V_T$ used on the measured $I_{D,Sat}^{0.5}$-$V_g$ characteristics. $V_T$ was extracted at its maximum slope point. Inset α displays the typical transfer characteristics of the devices under test with an applied drain-source bias ($V_D$) of -5 V. Such a $V_D$ was chosen for the $V_T$ extraction according to Inset β, the typical output characteristics of the devices under test at $V_g > V_T$, to ensure the device operation is in the saturation region (Supporting Information). (**b**) Representative $\Delta V_T$ (= $V_{T\ (with\ molecules)} - V_{T\ (without\ molecules)}$) of the devices under test extracted from both the forward (solid circle) and back (solid square) scans after the grafting of different molecular monolayers (**1**-**4**), as well as on the control samples. Data shown here is the average value for 14 devices identical to those in Figure 3. The vertical bars indicate standard deviations for each of the 14 devices tested.

The changes in $V_T$ after the monolayer molecular grafting are consistent with those in $I_D$. Attaching compounds **1**-**3** led to a more negative $V_T$ and less $I_D$ while attaching **4** resulted in a less negative $V_T$ and larger $I_D$. Therefore the channel conductances were reduced by grafting molecular monolayers of **1**-**3**, and they were increased by **4**, scaling directly with the relative electron donating ability of the molecules.

During the grafting process, hydrogen atoms on the H-passivated surface were replaced by the molecules and new aryl-silicon bonds were formed (Figure 2b). Some H-passivated sites remain due to steric constraints on the assembly, as seen by surface IR analysis.[13] Nevertheless, the resultant monolayers are dense enough to provide significant surface-passivation against electrochemical faradaic charging and they are even stable to short buffered oxide or KOH etching.[13] Based on this packing of molecules and on the observed electrical results, the mechanisms are discussed below.

A molecular monolayer with a positive dipole (here the sign of the molecular dipole is arbitrarily chosen to be positive if its negative pole points away from the surface after grafting) is induced by compounds **3** and **4**, while a negative dipole for **1** and **2**. Although it is realized that the resultant dipole layer on the surface can create an electrostatic potential that would produce effects similar to those induced by a gate bias in a standard MOSFET,[31] the model that the molecular monolayer acts as a top gate is not considered in our case because it cannot explain why **1** and **2** have the same effects as **3**, or why **3** and **4** (with the same dipole polarity) exhibit opposite effects. Furthermore, it seems unreasonable to simply add such a local field to the external field.

The fact that grafting molecular monolayers onto the channel region can change its conductance is mildly analogous, from a charge perspective, to that of the impurity doping. Considering an accumulation channel (p-channel) was formed in our pseudo-MOSFETs, the acceptor-like monolayer (more potent than the hydrogen atom of the H-passivated control) would decrease the $V_T$ of the pseudo-MOSFET and the donors would increase the $V_T$. Following this suggestion, the data implies that p-Si gained negative charges when modified by compounds **1**-**3**, while it gave up negative charges in the case of **4**. A simple calculation (Supporting Information) implies that a 1 V change in $V_T$ corresponds to the transfer of about 0.002 elementary charges per grafted molecule; a value consistent with electrostatic effects of organic molecules on neighboring bodies.[32] Such a charge transfer process is dependent on several factors. During the molecular assembly, Si-C bonds were formed between the aryl ring and lightly boron-doped silicon. The л-electron cloud from the aryl system is in close interaction with the silicon surface and thus the different molecular effects may originate from the functional group of the attached molecules. Since the functional groups of **1** ($-N(CH_3)_2$) and **2** ($-NH_2$) are donors, the density of this л-electron cloud is higher than that of **3** ($-NO_2$), an acceptor, and **4** (polymolybdate cluster) a potent acceptor.[33-36] So it is reasonable that, relative to the H-passivated surface, **1** and **2** act as the electron donor while **4** as the acceptor. This agrees with our experimental results. However, it can not explain the location of **3** in Figure 4b. Note this designation of acceptor for the $-NO_2$ moiety is relative to a hydrogen atom at the 4-position of a phenyl ring and here we are comparing a 4-nitrophenylene ($4\text{-}C_6H_4\text{-}NO_2$) as assembled in **3** to simply a hydrogen atom directly bonded to the silicon surface in the H-passivated control. The 4-nitrophenylene, with its л-electron cloud from the aryl system in close interaction with the silicon surface, may still be acting as an electron donor relative to the H-passivated

surface. It is not until we go to a very strong electron withdrawing groups as in the polymolybdate cluster **4** that we are able to shift the electron withdrawing effect sufficiently past that of the control surface. Indeed, nitrobenzene has a more negative reduction potential than that of the aryl polymolybdate cluster,[33-35] confirming **4** as the most potent acceptor in the series. This also explains why the change in $V_T$ was observed in the series **1** > **2** > **3** > **4**.

In addition, replacing the hydrogen atoms on the H-passivated surface by molecules may generate new surface states. It has been reported that surface or interface bands can modulate the thermal excitation of bulk carriers in thin silicon layers.[6] Since a dipole layer is present on the surface and considering the dipole-dipole interactions, additional charge redistribution at the surface or interface is induced.[25,37-39] This can also affect the charge transfer process. The dipole moment may be different from molecule to molecule. The tilt angle and coverage or density of the grafted molecules might also be quite different between the molecular group **1-3** (all being about the same molecular size) and molecule **4** (being relatively large and more difficult to pack). All of this leads to unique charge redistributions and the resulting molecular effects that depend on the relative structures of the grafted molecules and their resultant monolayers. Hence the charge-transfer process is closely related to the alignment of the molecular and surface energy levels in the devices.[2,40-42]

**Summary**

In this contribution we demonstrated that, by grafting a monolayer of molecules atop oxide-free H-passivated silicon surfaces (channel region), the drain current and threshold voltage in pseudo MOSFETs can be systematically modulated over a wide electronic range in accordance with the electron-donating ability of the grafted molecules. This effect is ascribed to the charge transfer between the device channel and the molecules. This could serve as an excellent method to controllably tune electronic performance in nanoscale devices (large surface-area-to-volume ratios) through surface grafting where consistent impurity doping becomes hard to achieve due to doping profile inhomogeneities between devices.

## REFERENCES


(1) Tour, J. M. *Molecular Electronics: Commercial Insights, Chemistry, Devices, Architecture and Programming*, World Scientific: River Edge, New Jersey, 2003.

(2) Seminario, J. M.; Araujo, R. A.; Yan, L. *J. Phys. Chem. B* **2004**, *108*, 6915-6918.

(3) Reed, M. A.; Lee, T. *Molecular Nanoelectronics*, American Scientific Publishers: Stevenson Ranch, 2003.

(4) Sze, S. M. *Semiconductor Devices: Physics and Technology*, ed. 2, Weley, New York, 2001.

(5) Ashkenasy, G.; Cahen, D.; Cohen, R.; Shanzer, A.; Vilan, A. *Acc. Chem. Res.* **2002**, *35*, 121-128.

(6) Zhang, P.; Tevaarwerk, E.; Park, B.; Savage, D. E.; Celler, G. K.; Knezevic, I.; Evans, P. G.; Eriksson, M. A.; Lagally, M. G. *Nature* **2006**, *439*, 703-706.

(7) Boland, J. J. *Nature* **2006**, *439*, 671-672.

(8) Yang, J.; de la Garza, L.; Thornton, T. J.; Kozicki, M.; Gust, D. *J. Vac. Sci. Technol. B* **2002**, *20*, 1706-1709.
(9) Shinada, T.; Okamoto, S.; Kobayashi, T.; Ohdomari, I. *Nature* **2005**, *437*, 1128-1131.
(10) Roy, S.; Asenov, A. *Science* **2005**, *309*, 388-390.
(11) Liu, Z. M.; Yasseri, A. A.; Lindsey, J. S.; Bocian, D. F. *Science* **2003**, *302*, 1543-1545.
(12) Ulman, A. *Chem. Rev.* **1996**, *96*, 1533-1554.
(13) Stewart, M. P.; Maya, F.; Kosynkin, D. V.; Dirk, S. M.; Stapleton, J. J.; McGuiness, C. L.; Allara, D. L.; Tour, J. M. *J. Am. Chem. Soc.* **2004**, *126*, 370-378.
(14) Hamers R. J.; Coulter, S. K.; Ellison, M. D.; Hovis, J. S.; Padowitz, D. F.; Schwartz, M. P.; Greenlief, C. M.; Russell, J. N., Jr. *Acc. Chem. Res.* **2000**, *33*, 617-624.
(15) Buriak, J. M. *Chem. Rev.* **2002**, *102*, 1271-1308.
(16) Brook, M. A. *Silicon in Organic, Organometallic, and Polymer Chemistry*, Wiley: New York, 2000.
(17) Katz, H. E. *Electroanalysis* **2004**, *16*, 1837-1842.
(18) Nikolaides, M. G.; Rauschenbach, S.; Bausch, A. R. *J. Appl. Phys.* **2004**, *95*, 3811-3815.
(19) Janata, J. *Electroanalysis* **2004**, *16*, 1831-1835.
(20) Maruccio G.; Visconti, P.; Biasco, A.; Bramanti, A.; Torre, A. D.; Pompa, P. P.; Frascerra, V.; Arima, V.; D'Amone, E.; Cingolani, R.; Rinaldi R. *Electroanalysis* **2004**, *16*, 1853-1862.
(21) Cahen, D.; Gartsman, K.; Kadyshevitch, A.; Naaman, R.; Shanzer, A. *Hybrid Organic-Inorganic Semiconductor Structures and Sensors Based Thereon*, US Patent, 6 433 356, 2002.
(22) Bartic, C.; Campitelli, A.; Borghs, S. *Appl. Phys. Lett.* **2003**, *82*, 475-477.
(23) Fritz, J; Cooper, E. B.; Gaudet, S.; Sorger, P. K.; Manalis, S. R. *PNAS* **2002**, *99*, 14142-14146.
(24) Becker, H. G. O.; K. Grossmann, *J. Prakt. Chem.* **1990**, *332*, 241-250.
(25) Milz, H.; Schladetsch, H. J. *Monodiazotization of aromatic diamines.* Ger. Offen., 15 pp., 1977.
(26) Dai, M. J.; Liang, B.; Wang, C. H.; Chen, J. H.; Yang, Z. *Org. Lett.* **2004**, *6*, 221-224.
(27) Cristoloveanu, S.; Williams, S. *IEEE Electron. Device Lett.* **1992**, *13*, 102-104.
(28) Terada, K.; Nishiyama, K.; Hatanaka, K. *Solid State Electron.* **2001**, *45*, 35-40.
(29) Schroder, D. K. *Semiconductor Material and Device Characterization*, ed.3, Wiley: Hoboken, 2006.
(30) Ortiz-Conde, A.; Sánchez, F. J. G.; Liou, J. J.; Cerdeira, A.; Estrada, M.; Yue, Y. *Microelectron. Reliab.* **2002**, *42*, 583-596.
(31) Cahen, D.; Naaman, R.; Vager, Z. *Adv. Funct. Mater.* **2005**, *15*, 1571-1578.
(32) Seminario, J. M.; Yan, L.; Ma, Y. *Proc. IEEE* **2005**, *10*, 1753-1764.
(33) Lu, M. ; Xie, B.; Kang, J.; Chen, F.; Yang, Y.; Peng, Z. *Chem. Mater.* **2005**, *17*, 402-408.
(34) Kang, J. ; Nelson, J. A.; Lu, M.; Xie, B.; Peng, Z.; Powell, D. R. *Inorg. Chem.* **2004**, *43*, 6408-6413.

(35) Donkers, R. L.; Workentin, M. S. *Chem. Eur. J.* **2001**, *7*, 4012-4020.
(36) Smith, M. B.; March, J. *Advanced organic chemistry: reactions, mechanisms, and structure*, ed.5, p.370, Wiley: New York, 2001.
(37) Hutchison, G. R.; Ratner, M. A.; Marks, T. J.; Naaman, R. *J. Phys. Chem. B* **2001**, *105*, 2881-2884.
(38) Selzer, Y.; Cai, L. T.; Cabassi, M. A.; Yao, Y. X.; Tour, J. M.; Mayer, T. S.; Allara, D. L. *Nano Lett.* **2005**, *5*, 61-65.
(39) Salomon, A.; Boecking, T.; Chan, C. K.; Amy, F.; Girshevitz, O.; Cahen, D.; Kahn, A. *Phys. Rev. Lett.* **2005**, *95*, 266807.
(40) Iozzi, M. F.; Cossi, M. *J. Phys. Chem. B* **2005**, *109*, 15383-15390.
(41) Natan, A.; Zidon, Y.; Shapira, Y.; Kronik, L. *Phys. Rev. B* **2006**, *73*, 193310.
(42) Cohen, R.; Kronik, L.; Shanzer, A.; Cahen, D.; Liu, A.; Rosenwaks, Y.; Lorenz, J. K.; Ellis, A. B. *J. Am. Chem. Soc.* **1999**, *121*, 10545-10553.

**Synthesis of the target molecules**

(**6**). A mixture of **5** (0.80 g, 0.5 mmol),[1] 4-iodophenyldiethyltriazene (0.13 g, 0.6 mmol), $Pd(PPh_3)_2Cl_2$ (10 mg, 0.01 mmol), CuI (6 mg, 0.02 mmol), $K_2CO_3$ (1.0 g, 7 mmol), triethylamine (0.5 mL of a 1M solution in acetonitrile) and acetonitrile (10 mL) was stirred at room temperature for 20 min under nitrogen. The resulting dark red solution was filtered. The filtrate was concentrated to about 3 mL and a solid was precipitated by adding diethyl ether. The orange precipitate was further purified by recrystallization several times from acetonitrile/diethyl ether to yield **6** (0.2 g, 0.14 mmol, 24%) as red crystals. MP 210 °C (dec). $^1$H NMR $CD_3CN$, 400 MHz, 25 °C) δ 7.47 (d, $J$ = 8.72 Hz, ArH, 2H), 7.37 (d, $J$ = 8.72 Hz, ArH, 2H), 7.22 (s, ArH, 2H), 3.78 (q, $J$ = 7.08 Hz, $NCH_2$, 4H), 3.08 (t, $J$ = 8.72 Hz, $NCH_2$, 16H), 2.60 (s, $ArCH_3$, 6H), 1.60 (q, $J$ = 7.94 Hz, $CH_2$, 16H), 1.35 (h, $J$ = 7.25 Hz, $CH_2$, 16H), 1.28 (b, $CH_3$, 6H), 0.96 (t, $J$ = 7.25 Hz, $CH_3$, 24H). IR ($cm^{-1}$) 2691, 2872, 2198, 1655, 1587, 1481, 1464, 1392, 1328, 1237, 978, 952, 778, 553, 464.

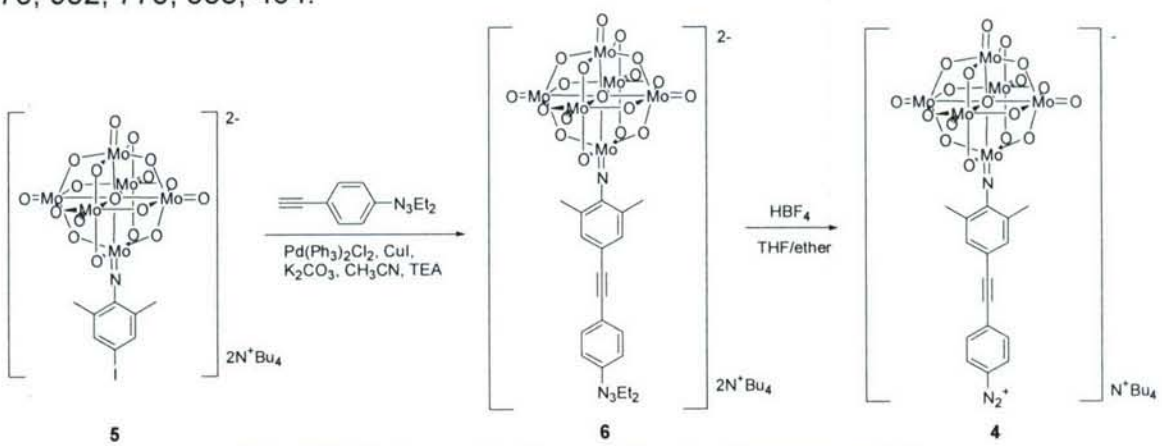


**5** **6** **4**

**Fig. S1** Scheme for the synthesis of compound **4**.

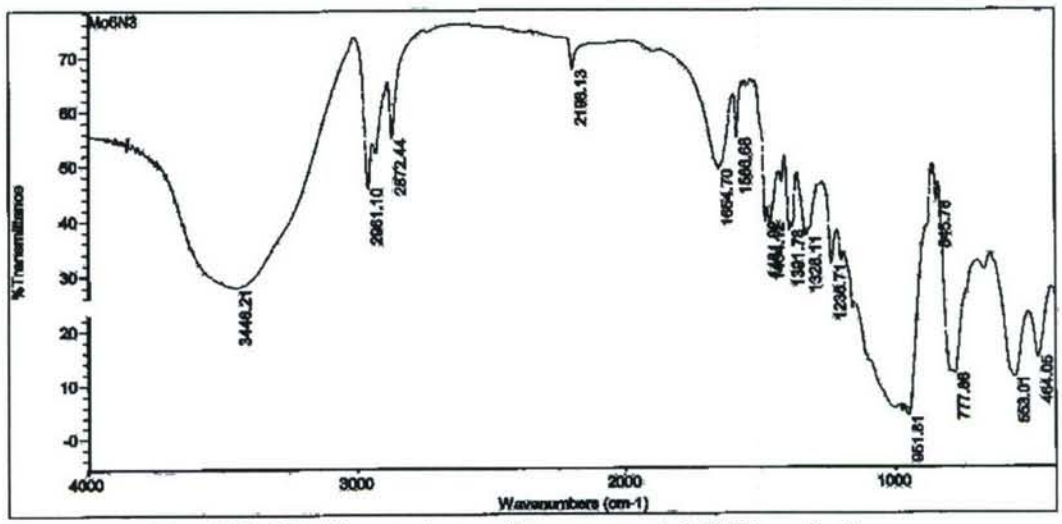


**Fig. S2** FT-IR spectrum of compound **6** (KBr pellet).

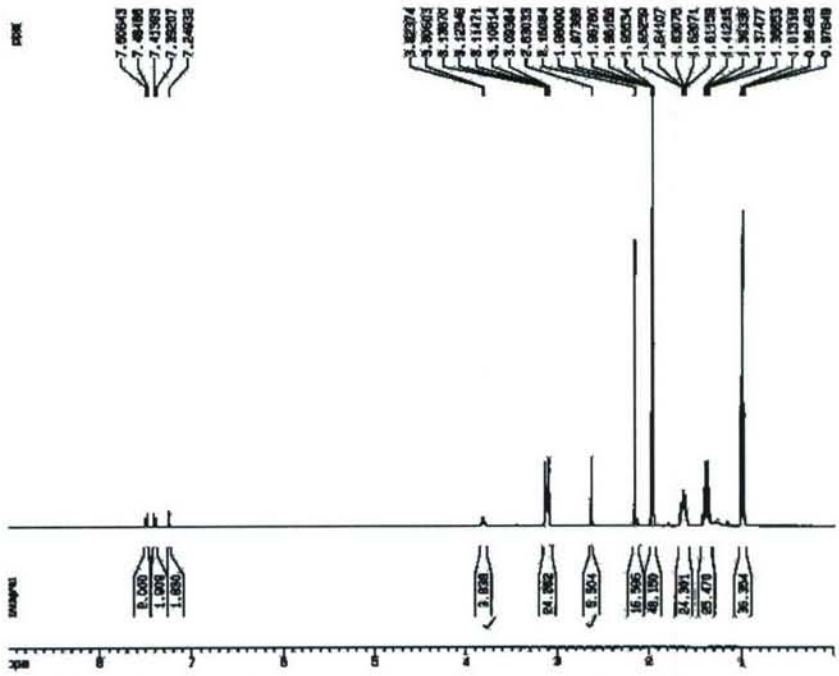


**Fig. S3** $^1$H NMR spectrum of compound **6** in $CD_3CN$.

**(4)**. To a 10 mL vial was added **6** (50.0 mg, 0.03 mmol) and THF (1 mL). $HBF_4$ (5% solution in water, 0.13 mL) was then added dropwise under nitrogen. After stirring for 2 min, diethyl ether (5 mL) was added and an orange precipitate was formed. The precipitate was collected and washed with diethyl ether, then dried under nitrogen to give **4** as an orange solid (36.0 mg, 0.02 mmol, 65%). Note that the cluster portion has a -2 charge while the diazonium portion has a +1 charge, making the molecule have an overall -1 charge that is balanced by the lone $N^+Bu_4$ evident in the $^1$H NMR. $^1$H NMR ($CD_3CN$, 400 MHz, 25 °C) δ 8.48 (d, $J$ = 8.50 Hz, ArH, 2H), 7.81 (d, $J$ = 8.50 Hz, ArH, 2H), 7.29 (s, ArH, 2H), 3.08 (t, $J$ = 8.72 Hz, $NCH_2$, 8H), 2.54 (s, $ArCH_3$, 6H), 1.60 (q, $J$ =

7.94 Hz, $CH_2$, 8H), 1.35 (h, $J$ = 7.25 Hz, $CH_2$, 8H), 0.96 (t, $J$ = 7.25 Hz, $CH_3$, 12H). IR ($cm^{-1}$) 2959, 2871, 2242, 2190, 1568, 1457, 1379, 1313, 1237, 1078, 976, 950, 776, 590, 442.

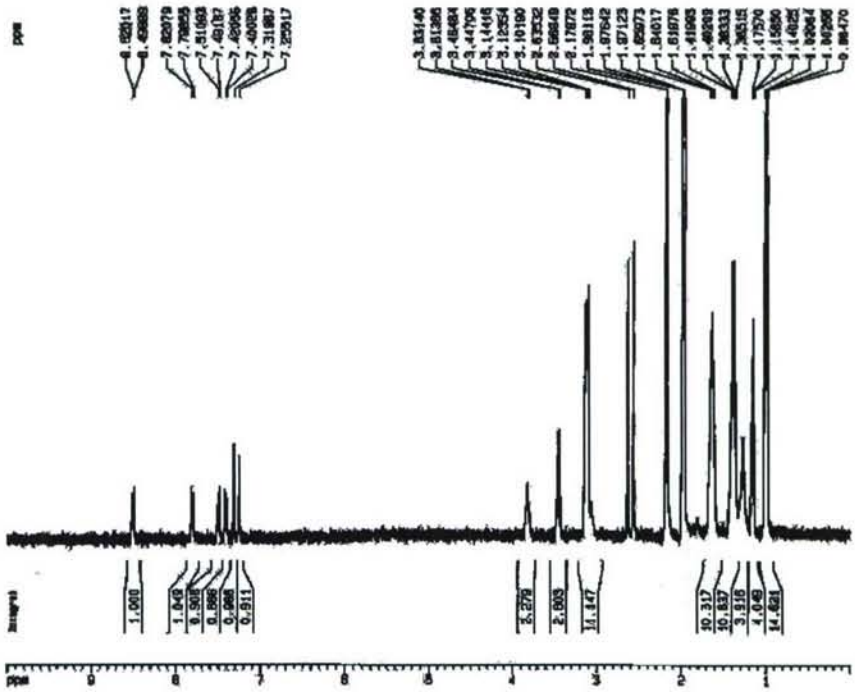

**Fig. S4** $^1$H NMR spectrum of compound **4** in $CD_3CN$.

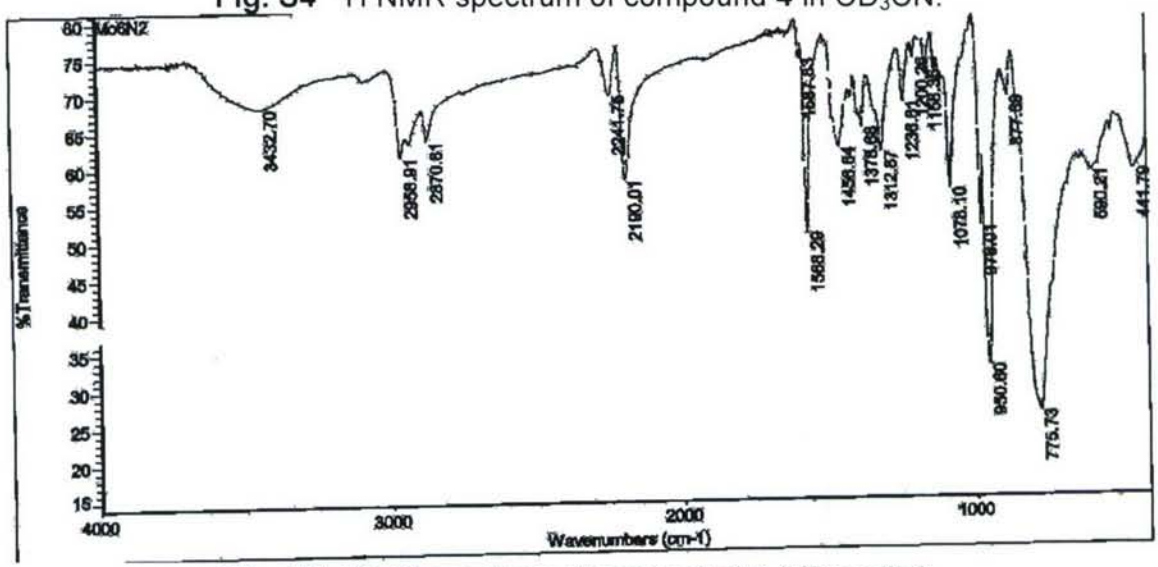


**Fig. S5** FT-IR spectrum of compound **4** (KBr pellet).

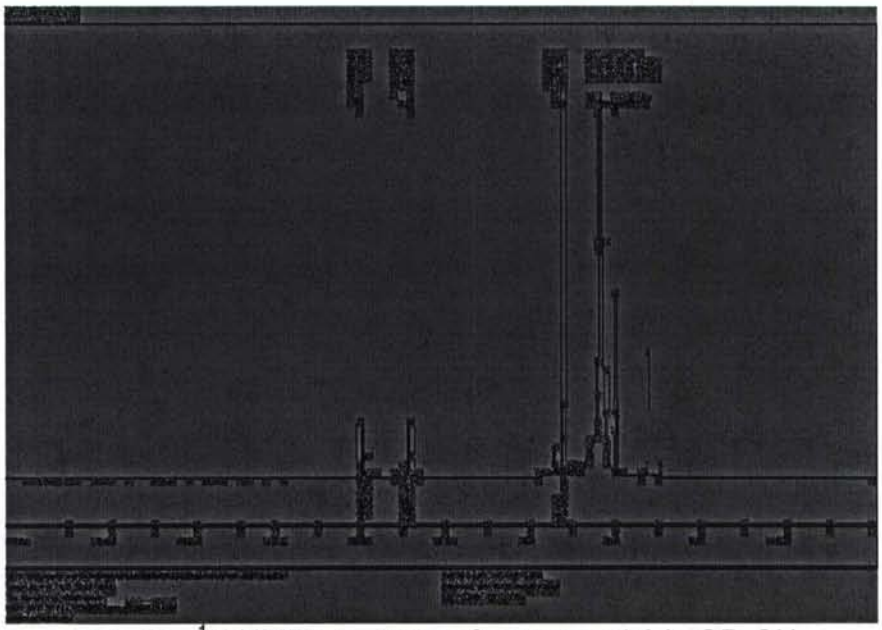

**Fig. S6** $^1$H NMR spectrum of compound **1** in $CD_3CN$.

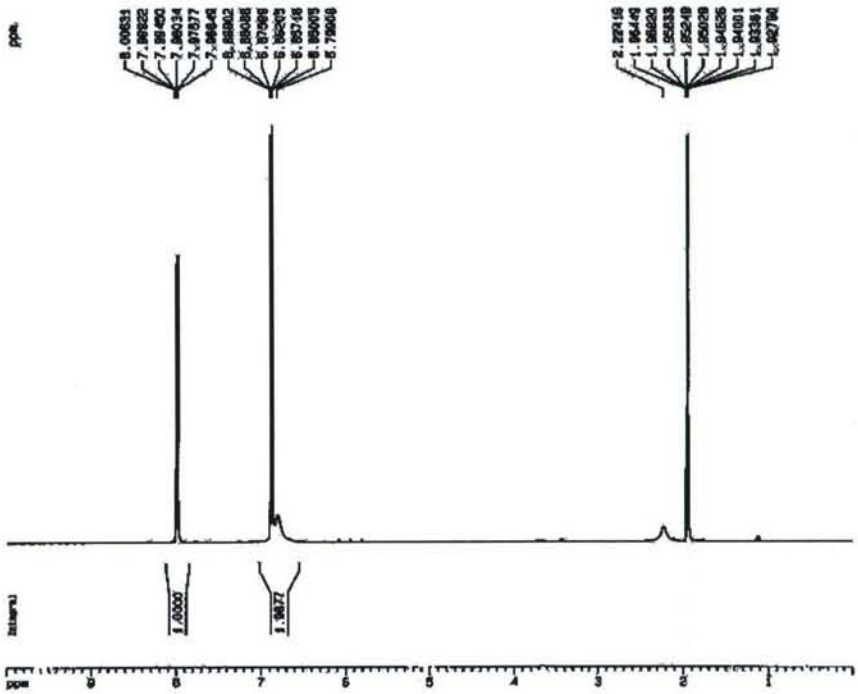

**Fig. S7** $^1$H NMR spectrum of compound **2** in $CD_3CN$.

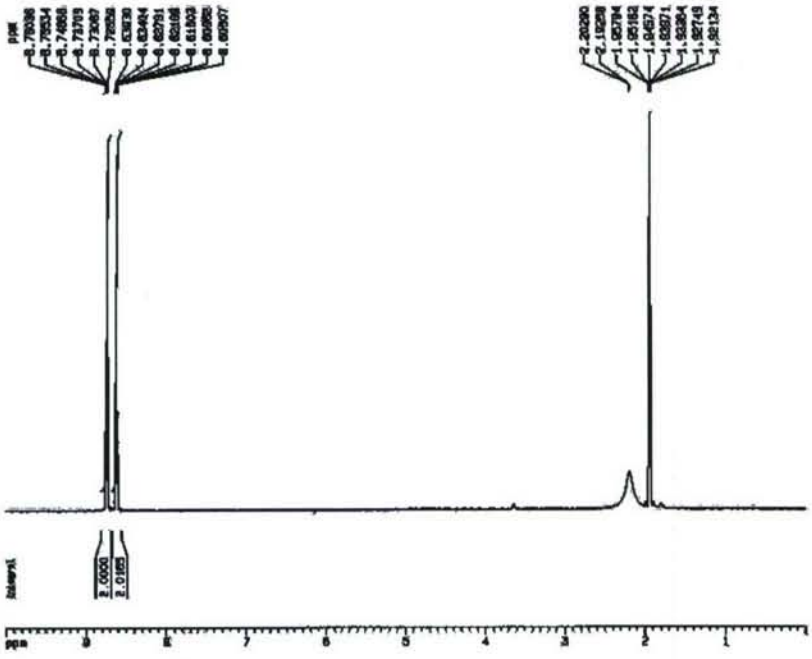

**Fig. S8** $^1$H NMR spectrum of compound **3** in $CD_3CN$.

**Part II. XPS and ellipsometric characterization of the silicon grafted with molecules (1-4)**

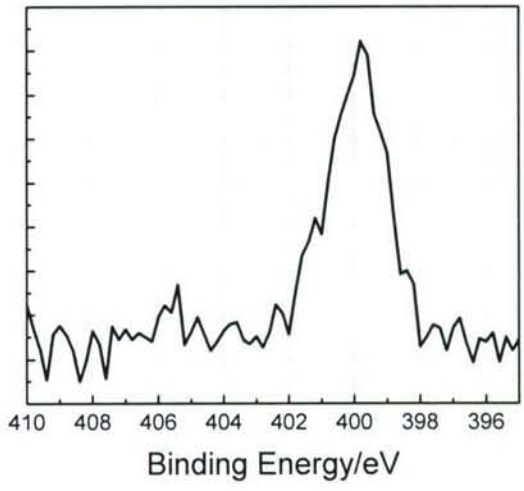


**Fig. S9** Representative *N*1s XPS spectrum for the molecular layer formed from compound **2**. Compound **1** displays a very similar *N*1s XPS spectrum with a slight shift of the peak. This indicates the molecules **1** and **2** were grafted on the silicon surface.

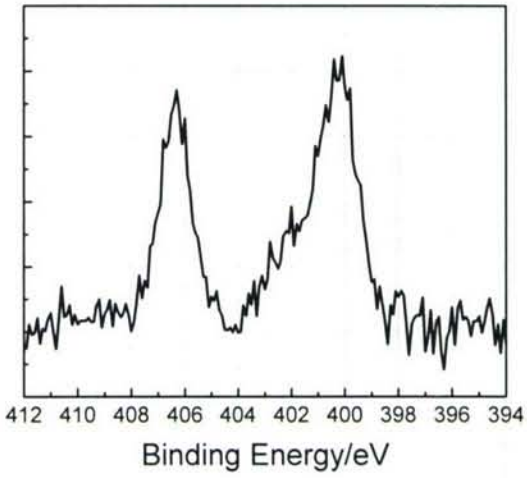


**Fig. S10** Representative *N*1s XPS spectrum for molecular layer formed from compound **3**, indicating the molecules were grafted on the silicon surface.

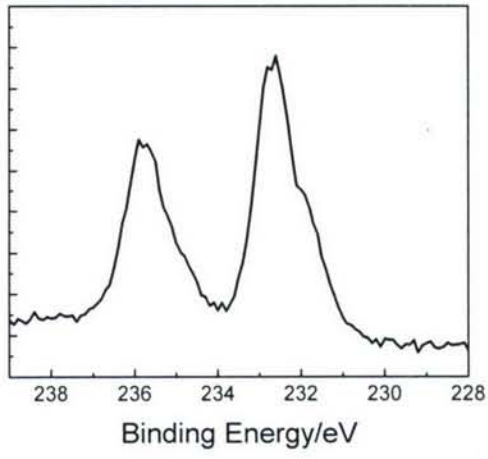


**Fig. S11** Representative *Mo*3d XPS spectrum for the molecular layer formed from compound **4**, indicating the molecules were grafted on the silicon surface.

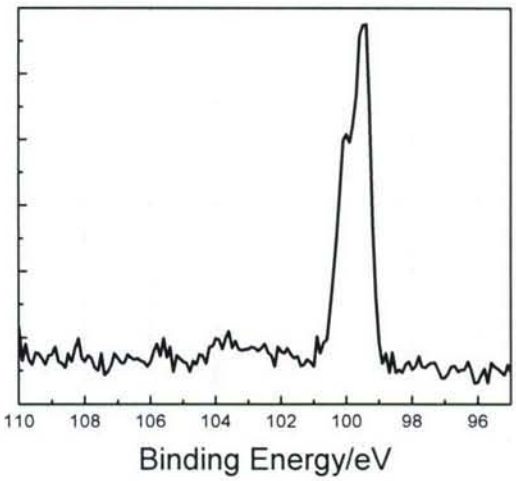


**Fig. S12** Typical *Si*2p XPS spectrum for the samples after etching or after molecular grafting. The analysis indicates there was no silicon oxide layer present on the surface after etching or after molecular assembly since there was no typical peak for silicon oxide, which would appear at about 103 eV.

**Table S1** Ellipsometric thickness of the molecular layer formed on the silicon surface by the precursor compounds and the theoretical molecular length, indicating that a molecular monolayer was formed on the surface.

| Precursor Compound | | **1** | **2** | **3** | **4** |
|---|---|---|---|---|---|
| Film thickness (nm) | Measured (±5%) | 0.83 | 0.9 | 0.9 | 1.89 |
| | Calculated | 0.85 | 0.8 | 0.8 | 1.85 |

**Part III. Definition and extraction of the threshold voltage in MOSFETs**

Though it has been given various definitions, threshold voltage ($V_T$) may be understood as the gate voltage value at which the transition between weak and strong inversion takes place in the MOSFET channel.[2] The definition of $V_T$ suggested here is now commonly used, which is that gate voltage for which the surface potential, $\Phi_S$, in the semiconductor below the gate oxide is given by supplementary equation 1.

$$\Phi_S = 2\Phi_F = \frac{2kT}{q} In(\frac{p}{n_i}) \approx \frac{2kT}{q} In(\frac{N_A}{n_i}) \quad (1)$$

where $\Phi_F$ is the Fermi potential, $q$ the electron charge, $k$ Boltzmann's constant, $T$ the temperature, $p$ hole density, $n_i$ intrinsic carrier density, and $N_A$ acceptor doping density. This definition is based on equating the surface minority carrier density to the majority carrier density in the neutral bulk, i.e., $n$(surface) = $p$(bulk). Thus, for large-geometry, n-channel devices on uniformly doped substrates with no short- or narrow-channel effects, when measured from gate to source, $V_T$ is given by supplementary equation 2.

$$V_T = V_{FB} + 2\Phi_F + \frac{\sqrt{2qK_S\varepsilon_0 N_A(2\Phi_F - V_{BS})}}{C_{OX}} \quad (2)$$

where $V_{BS}$ is the substrate-source voltage, $V_{FB}$ the flatband voltage, $K_s$ the semiconductor dielectric constant, $\varepsilon_0$ the permittivity of free space and $C_{ox}$ the oxide capacitance.[3]

Among the numerous methods of extraction of the $V_T$ value,[4-6] in light of the relatively low drain current under low drain-source bias ($V_D$), we used the extrapolation method in the saturation region. The $V_T$ was determined from the gate voltage ($V_g$) axis intercept of the $I_{D,Sat}^{0.5}$-$V_g$ characteristics linearly extrapolated (see Figure 4a in the main text). To minimize the influence of the source and drain parasitic series resistances and the channel mobility degradation on the resulting value of the extracted $V_T$, the extrapolation was done at its maximum first derivative (slope) point.[5,6] We also tried the extraction methods based on the device operation in the linear region, such as the one from the intercept with the $V_g$ axis of the straight line fit of $I_D/g_m^{0.5}$-$V_g$ characteristics ($g_m$ is the transconductance), which was developed to avoid the dependence of the extracted $V_T$ value on mobility degradation and parasitic series resistance.[6-8] The same trend for the change in $V_T$ before and after molecular grafting was observed using different extraction methods, though the extracted $V_T$ values were slightly different. Although we also determined the results using the device operation in the linear region, the $V_T$ values shown in this contribution were thus extracted by using the method based on the device operation in the saturation region (see Figure 4a in the main text).

**Part IV. Output characteristics of the pseudo-MOSFET devices**

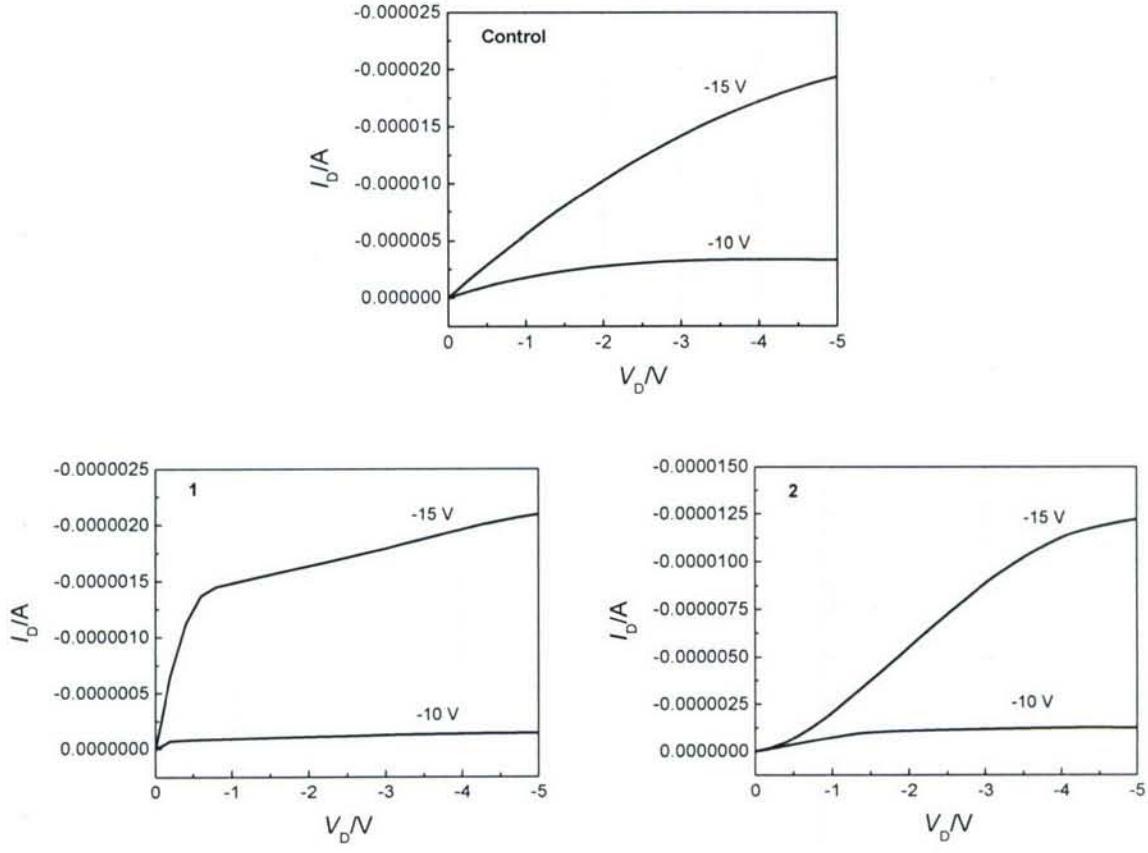

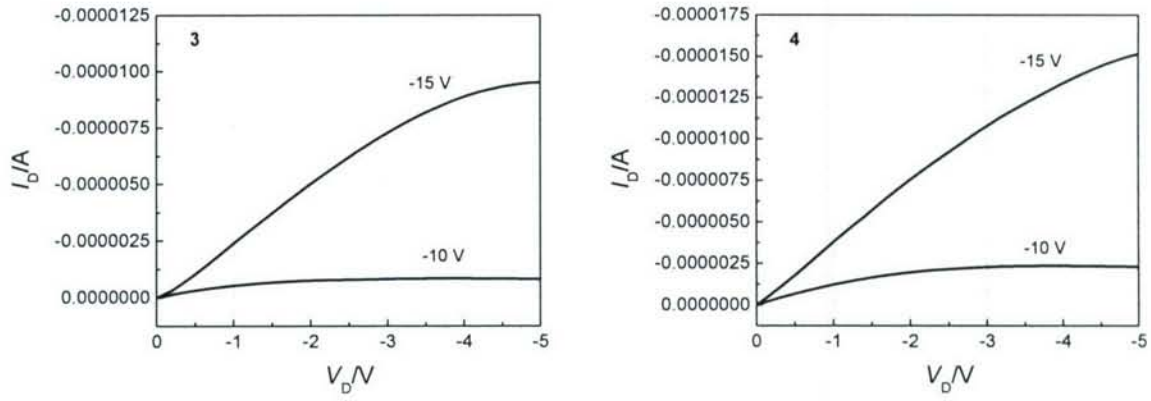


**Fig. S13** Typical output characteristics of the devices under test and the sample control. The numbers (1, 2, 3 and 4) in the illustrations correspond to the compounds **1-4**, respectively. According to the above figures the $V_D$ was chosen to be -5 V for the $V_T$ (less negative than -10 V) extraction in order to ensure the device operation was in the saturation region.

## Part V. Simple calculation about the charge transfer between p-Si and grafted molecules

Given the thickness of the gate silicon oxide (1000 nm) and its dielectric constant (3.9), the capacitance of the gate is calculated to be $3.45 \times 10^{-9}$ F·cm$^{-2}$ using supplementary equation 3.

$$C_{ox} = \frac{\varepsilon_r \varepsilon_0}{l} = \frac{3.9 \times 8.85 \times 10^{-14}}{1000 \times 10^{-7}} = 3.45 \times 10^{-9} (Fcm^{-2}) \quad (3)$$

Such a capacitance means that one volt change in the gate would correspond to $2.16 \times 10^{10}$ elementary charges per cm$^{-2}$. The assembly area per device in Row 0 is $1.21 \times 10^{-4}$ cm$^2$. Thus one volt change of $V_T$ would imply about $2.61 \times 10^6$ carriers involved. Assuming the coverage or density of the grafted molecules is $10^{13}$ cm$^{-2}$, this suggests that there are $1.21 \times 10^9$ molecules per device. Therefore one volt change of $V_T$ corresponds to the transfer of about $2.0 \times 10^{-3}$ elementary charges per molecule ($2.61 \times 10^6$ divided by $1.21 \times 10^9$).

## Part VI. Supplementary References

(S1) Wei, Y.; Xu, B.; Barnes, C. L.; Peng, Z. *J. Am. Chem. Soc.* **2001**, *123*, 4083.
(S2) Brown, W. L. *Phys. Rev.* **1953**, *91*, 518.
(S3) Feldbaumer, D. W.; Schroder, D. K. *IEEE Trans. Electron. Devices* **1991**, *38*, 135.
(S4) Terada, K.; Nishiyama, K.; Hatanaka, K. *Solid State Electron.* **2001**, *45*, 35.
(S5) Schroder, D. K. *Semiconductor Material and Device Characterization*, ed.3, Wiley: Hoboken, 2006.
(S6) Ortiz-Conde, A.; Sánchez, F. J. G.; Liou, J. J.; Cerdeira, A.; Estrada, M.; Yue, Y. *Microelectron. Reliab.* **2002**, *42*, 583.
(S7) Fikry, W.; Ghibaudo, G.; Haddara, H.; Cristoloveanu, S.; Dutoit, M. *Electron Lett.* **1995**, *31*, 762.
(S8) Mourrain, C.; Cretu, B.; Ghibaudo, G.; Cottin, P. Proceedings of the 2000 International Conference on Microelectronic Test Structures (ICMTS), 2000 181.

## Neutral Complexes of First Row Transition Metals Bearing Unbound Thiocyanates and Their Assembly on Metallic Surfaces


### Abstract

A series of transition metal coordination complexes designed to assemble on gold surfaces was synthesized, their electronic structure and transitions analyzed, and their magnetic properties studied. By taking advantage of recently developed thiocyanate assembly protocols, these molecules were then assembled onto a gold surface, without the need for an inert atmosphere, to give a loosely packed monolayer. This molecular assembly was designed for and used in single molecule transistors (SMTs).


### Introduction

Watershed events for the molecular electronics community were the measurements of single molecule conductance by several groups.[1-7] Following these demonstrations, scientists began to propose and measure electronic behavior attributed to single or small ensembles of molecules. Significant recent contributions to this field include papers on the Kondo effect[8-10] and inelastic electron tunneling spectroscopy (IETS)[11-14] in individual molecules. These papers explored quantum phenomenon[15-18] in individual molecules that were part of metal-molecule-metal junctions. These analyses supported the concept of molecular devices and also provided a bridge connecting traditional synthetic and analytical chemistry with molecular electronics.

We have extended this work by synthesizing a new series of metal-containing molecules. The purpose of the metal core is two fold. First, one can discern which electronic effects in the junction are due to the metal atom core by varying the metal. Second, one can study the effect of different spin states on molecular conductance. Here we describe the efficient synthesis of these molecules and the simple techniques necessary for assembling them along with detailed characterization data of the assembled compounds on gold surfaces. From these data we can determine with high confidence the nature of the molecules after assembly. These compounds were also studied in electromigration-fabricated single molecule transistors (SMT) (Figure 1a). Some discussion of SMT results relevant to molecular properties are disclosed here, however, in-depth analyses of these results are found elsewhere.[13,19-21]

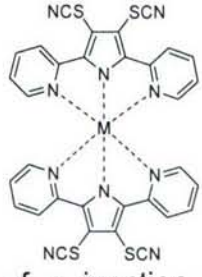


**1** M=Zn
**2** M=Cu
**3** M=Ni
**4** M=Co
**5** M=Fe

**Figure 1.** (a) A SEM image of a junction used in the testing of the molecular devices.[13,19,20] (b) The targeted molecular systems synthesized for this study.

The compounds **1**-**5** (Figure 1b) were synthesized with several parameters in mind. First, these molecules were designed to have a simple assembly protocol on metal where they are stable to air yet active towards a metal surface without the use of exogenous reagents. We have taken advantage of our recently published thiocyanate assembly procedure, in which the thiocyanate is converted to a thiolate via the gold surface, and the cyanide leaves as $[Au(CN)_2]^-$.[22,23] Thus, the metal complexes spontaneously assemble on a clean gold surface (Figure 2). Use of the thiocyanates eliminates the need for the oxidatively unstable aromatic free thiols or their thioacetate precursors.[24-26]

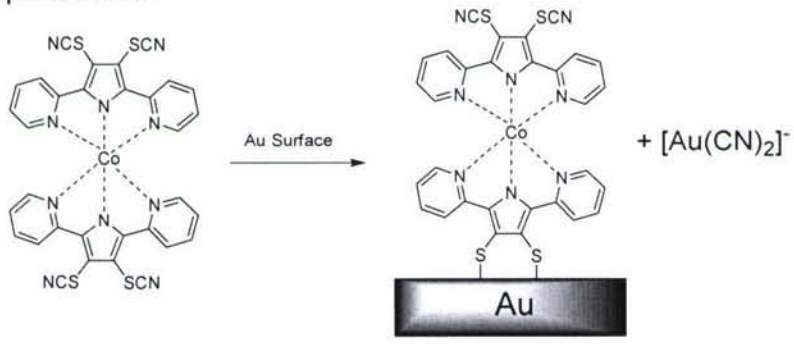


**Figure 2.** Schematic of the assembly on gold.

When designing these molecules we wanted to avoid parasitic charges that may interfere with electrical studies, and thus designed the system to be overall neutral (no counter ions). In order to facilitate molecular conduction, the molecule was designed to be small and contain a continuous π-electron system that is interrupted only by the core in order to force electrons through the metal atom. Finally, the molecules were designed such that all coordination sites on the metal atom were bound by multi-dentate ligands. This is important since it minimizes ligand dissociation and retards effects that may influence electrical studies, such as decomplexation, ligand exchange, or complexation of trace species such as water. Occupation of all coordination sites is also essential as these molecules are designed to contain a moiety (sulfur) for binding to metal surfaces in the presence of a metal core. If there were free coordination sites they could lead to complexation of the sulfur with the metal core. The two tridentate ligands therefore protect the molecule from self decomposition.

## Experimental

*Materials.* The syntheses of all compounds can be found in the supporting information, along with characterization including: $^1H$, $^{13}C$, IR (powder and surface), magnetic susceptibility, EPR, CV, UV-vis, DSC, TGA, MS, elemental analysis, and XPS (power and surface). Ethanol (100%) was obtained from Pharmco. THF was freshly distilled (sodium, benzophenone) prior to use. Dichloromethane was distilled from calcium hydride. All metals were of 99.99% or greater purity. Silicon <100> wafers (p doped, test grade) were obtained from Silicon Quest International. Gold coated mica was purchased from Molecular Imaging.

*EPR.* All EPR samples were prepared by dissolving the metal complexes in freshly distilled THF (ca. 10 μM, **2**; 100 μM, **4**). Solution were passed through a 0.2 μm nylon

filter and then quickly frozen. Spectra were taken in a Varian E6 X-band spectrometer with an Air Products helium cryogenic system.

*Magnetic Susceptibility.* Magnetic susceptibility measurements were taken in a Superconducting Quantum Interference Device (SQUID). Analysis was carried out at temperatures from 300 K to 1.7 K using a Quantum Design MPMS-5S magnetometer.

*Cyclic Voltammetry.* Electrochemical characterization was carried out with a Bioanalytical Systems (BAS CV-50W) analyzer. The reference was a $Ag|AgNO_3$ electrode. The counter electrode was a clean Pt wire. Redox potentials were determined at the specified scan rates. The solutions studied were 1 mM with 0.1 M tetrabutylammonium tetrafluroborate as the supporting electrolyte in THF under inert atmosphere.

*UV-Visible absorbance.* UV-vis spectra were acquired on a Shimadzu UV-3101PC containing both a deuterium and halogen light source. All spectra were collected in freshly distilled dichloromethane.

*Preparation of Evaporated Metal Substrates.* All metal substrates were prepared by thermal evaporation with a base pressure of ~1 x $10^{-6}$ Torr on test grade <100> silicon wafers with a typical evaporation rate of 1 Å/s. A chromium adhesion layer (5 nm) was applied to all substrates prior to deposition of 150 nm of the metal. All substrates were used within 20 min after removal from the vacuum chamber.

*Assembly Procedure.* Molecules were assembled onto freshly prepared substrates in freshly distilled dichloromethane or THF at a concentration of 0.5-1.0 mM. Assemblies typically proceeded for 24 h in the dark, after which they were vigorously rinsed with the same solvent used for assembly and dried under a stream of nitrogen.

*Ellipsometric Measurements.* Measurements of surface optical constants and molecular layer thicknesses were taken with a single wavelength (632.8 nm laser) LSE Stokes Ellipsometer (Gaertner Scientific). The surface thickness was modeled as a single absorbing layer atop an infinitely thick substrate (fixed $n_s$). The observed error in repeated measurements of the same spot was typically 0.2 nm or less. The index of refraction was set at 1.55.

*Infrared Reflection Spectroscopy Measurements.* A Nicolet Nexus 670 spectrometer with KBr beam splitter and MCT/A detector was used in conjunction with a SMART/SAGA grazing angle accessory, using a 16 mm diameter sampling area with p-polarized light fixed at an 80° angle of incidence.

*X-ray Photoelectron Spectroscopy (XPS) Measurements.* A PHI Quantera SXM XPS/ESCA system at 5 × $10^{-9}$ Torr was used to take photoelectron spectra. A monochromatic Al X-ray source at 100 W was used with an analytical spot size of 0.15 mm x 1.4 mm and a 45° takeoff angle, with pass energy of 26.00 eV. High resolution spectra of the S 2p region used a 45° takeoff angle and 13.00 eV pass energy. Unless

noted, surface samples were referenced against internal Au $4f_{7/2}$ line at 84.0 eV. Crystalline powder samples were referenced externally to an Au 4f peak at 84.00 eV and internally to a C 1s binding energy of 284.50 eV (NIST XPS database). Atomic concentration values were calculated with PHI Multipak software using factory calibrated values for the sensitivity factors of the respective elements.

**Synthesis**

The basic design was to have metal(II) surrounded by two anionic ligands (Figure 1b). Hence a ligand such as **8** was a natural choice (Scheme 1). Though this ligand had been synthesized previously[27] and even complexed on one occasion,[28] we found all previous methods to be impractical for large scale synthesis. Thus our preferred route to **8** begins with succinic acid that was converted to the bis-acetimide **6** in 89% yield using a slightly modified version of Schindlbauer's method.[29] This was then converted to the bis-pyridal system **7** with a modification of conditions outlined by Owsley.[30] Cyclization using ammonium acetate[27] gave **8**. This ligand was deprotonated and reacted with $ZnCl_2$ and $CoCl_2$ to produce **9** and **10** as test cases for the complexation (Scheme 2).

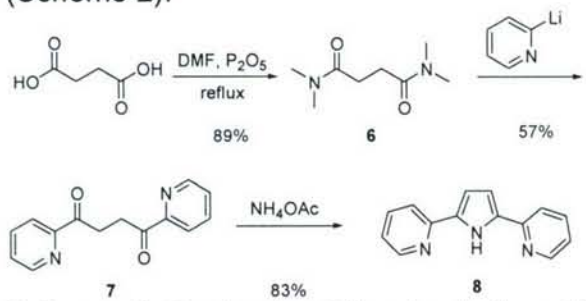


**Scheme 1**. Synthesis of the simple ligand **8**.

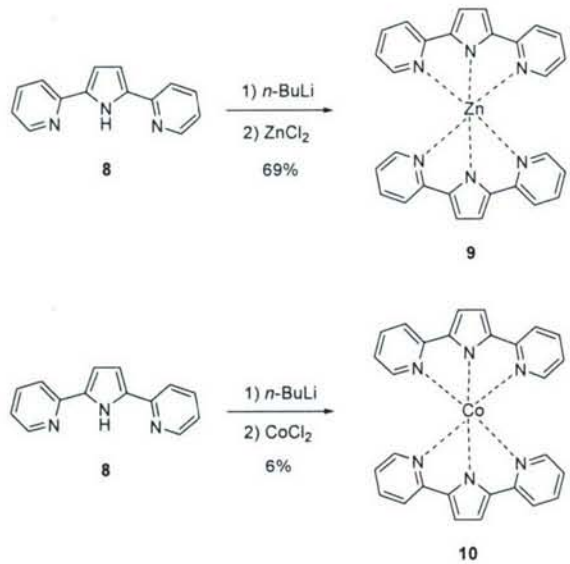


**Scheme 2.** Formation of the metal complex test cases.

With complexation successfully demonstrated, the possible methods for attachment of the molecules to metal surfaces were examined. The 4-positions of the pyridine rings and 3,4-positions of the pyrrole ring both suggest themselves as viable sites for functional groups that will attach to the surface.[31] We focused on substitution at the 3- and 4-positions of the pyrrole ring.

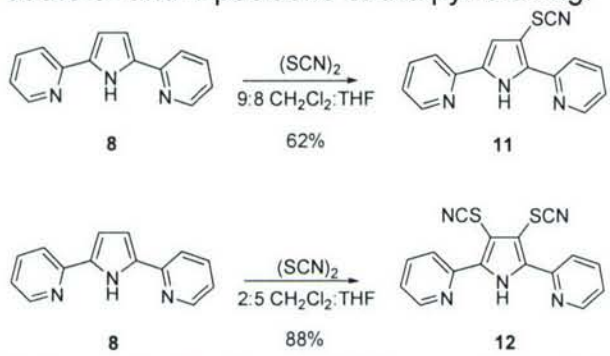


**Scheme 3**. Synthesis of thiocyanate-containing ligands. Solvent conditions determine whether the mono or dithiocyanate species is preferentially formed.

Thiocyantes were chosen as surface-binding precursors since they offer many of the advantages of the thiol on gold chemistry (such as rearrangement on a surface,[32] an important factor for such a bulky molecule) without the oxidative instability found in the free thiols.[25] This system has the advantage of not requiring any extraneous materials or inert conditions, and gives the same structure on gold as an assembly from a free thiol (Figure 2).

Accordingly, the mono and dithiocyanate functionalized ligands **11** and **12** were synthesized by treating the bare ligand with thiocyanogen ($(SCN)_2$, generated from $Pb(SCN)_2$ and $Br_2$). In a mixture of 9:8 $CH_2Cl_2$:THF the monothiocyanate **11** was formed preferentially while in a more polar mixture (2:5 $CH_2Cl_2$:THF) the major product was the dithiocyanate **12** (Scheme 3). For complexation, **12** was deprotonated with NaH, and then combined with the metal halide to give the final metal complexes **1-5** in varying yield. The iron compound **5** was meta-stable, allowing only partial characterization (Scheme 4).

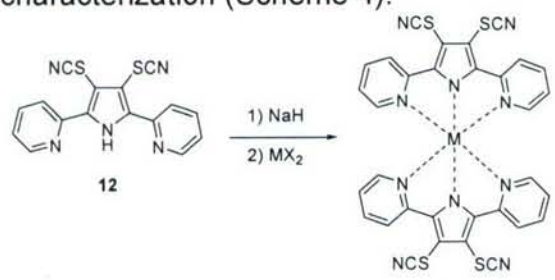


| Metal salt | Product | Yield (%) |
|---|---|---|
| $ZnCl_2$ | **1** | 91 |
| $CuBr_2$ | **2** | 72 |
| $NiBr_2$ | **3** | 43 |
| $CoCl_2$ | **4** | 72 |

| | | |
|---|---|---|
| $FeCl_2$ | **5** | 15 |

**Scheme 4.** Complexation of the free ligand **12** with the metal halide.

**Metal Complex Characteristics**

The metal complexes are intended to be studied in a variety of molecular electronic testbeds.[33] The results of the tests will be correlated with spectroscopic data to show these individual molecular effects in electronic devices.[11-13,20] The physical characterization data discussed here will focus primarily on molecular properties that will contribute to the discussion of the SMT data. An expansive version of the characterization can be found in the supporting information.

*Structure and Crystal Field Splitting*

The target compounds **1-5** share the same geometry. The complexes can be called compressed octahedra, an uncommon species[34,35] (Table 1, Figure 3). On average the $M\text{-}N_{pyrrole}$ bond distances (along the Z axis) are 0.2-0.3 Å shorter than the $M\text{-}N_{pyridine}$ bond distances. For a compressed octahedral species, it is common to predict the crystal field splitting based from an $O_h$ symmetry with the appropriate distortions noted (taking into account only the immediate environment of the metal[36]). The extent of tetragonal distortion (T, where $T=R_S/R_L$)[37] is not unusually large (0.84-0.89) and supports treatment of the complexes as compressed octahedra. Asymmetry that is not consistent with compressed octahedra is observed in the bond angles. The rigidity of the ligand results in N-M-N bond angles which deviate from 90° (average of 74-76°). This is only slightly larger than the typical Jahn-Tellar distortion commonly seen for coordination compounds including $Cu(dien)_2(NO_3)_2$ (79-80°), one of the few well studied compressed octahedral compounds,[37-39] which will serve as the basis for comparison in our work. Though the true symmetry of the molecule is $S_4$, the symmetry elements are similar to $D_{4h}$, and thus much of the literature can be used interchangeably.

| Metal | $R_S$ (Å) | $R_L$ (Å) | Avg. N-M-N angle (°) |
|---|---|---|---|
| Zn (**1**) | 1.96 | 2.32 | 74 |
| Cu (**2**) | 1.89 | 2.26 | 75 |
| Ni (**3**) | 1.96 | 2.23 | 76 |
| Co (**4**) | 1.97 | 2.24 | 74 |
| Fe (**5**) | 2.03 | 2.27 | 74 |

**Table 1**. Bond distance and angle deviations from $O_h$ symmetry.

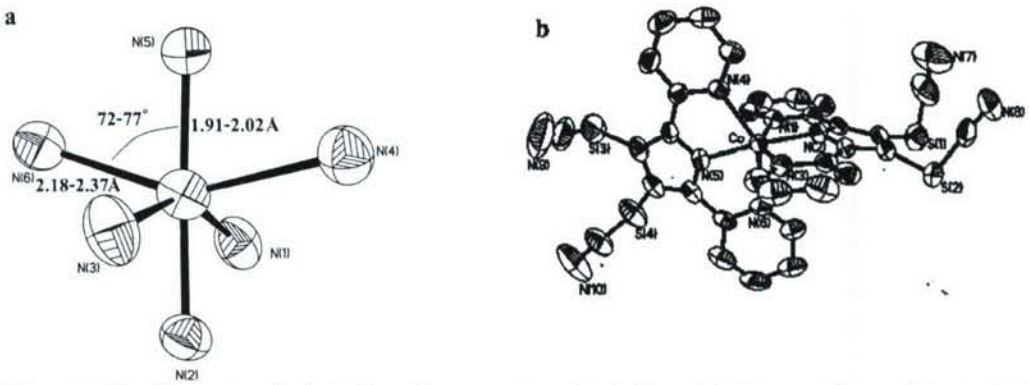


**Figure 3**. Structural details of compounds **1-5**. (a) The relevant bond distances and angles of **1-5**. (b) ORTEP of **4** from X-ray crystallography.

The crystal field splitting expected from $S_4/D_{4h}$ symmetry is illustrated in Figure 4. The splitting (and the associated transitions in the UV-vis spectrum) is somewhat ambiguous. The $d_{z^2}$ orbital is the highest in energy (by EPR spectroscopy vide infra), lying above the $d_{x^2-y^2}$ orbital. It is generally accepted[34,39,40] that the $d_{xz}$ and $d_{yz}$ orbitals lie at a slightly higher energy than the $d_{xy}$ orbital, though there has been some question as to the latter assignment.[38] Since we have no experimental evidence to suggest otherwise, we use the standard ordering (Figure 4).

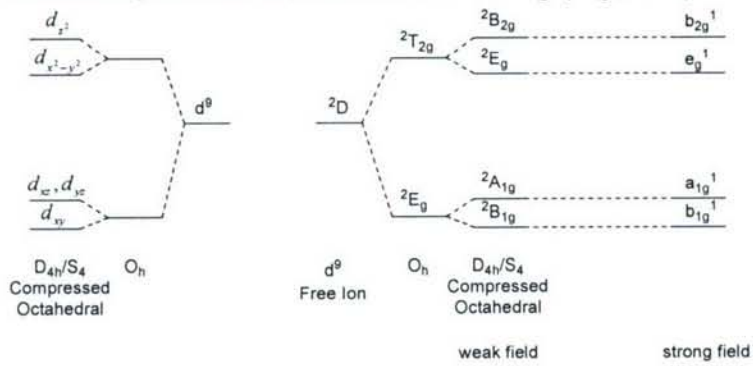


**Figure 4**. Crystal field splitting and correlation diagram for **2**.

*UV-Vis 43000-6250 cm$^{-1}$ (230-1600 nm)*

Building on the preceding discussion of the relative energies of the d orbitals, we examined the various d electron transitions in complexes **2-5**. The assignments of the absorption features of **2** are relatively straight forward (Table 2), and are consistent with the expected transitions. Assignments for the other metals are problematic. For nickel(II) ($d^8$), the correlation diagram gets more complex (Figure 5a) with 11 different terms for $O_h$ symmetry and 19 when $S_4$ symmetry is taken into account. Cobalt(II) ($d^7$) has seven free ion terms, and 19 in the simple case of $O_h$ symmetry. Thus the cobalt spectrum generally contains many broad indistinguishable features that can only be resolved at very low temperatures.[41,42]

Nickel has been studied in greater detail although low temperature is again necessary for full detailed studies of this system. For nickel we would expect three

main sets of transitions ($O_h$ symmetry) corresponding to the spin allowed transitions ($^3A_{2g}$ to $^3T_{2g}$, $^3T_{1g}$, and $^3T_{1g}$ (P)) (Figure 5). Each of these transitions will be split into two bands when the $S_4$ symmetry is taken into consideration. The transitions to $^3B_{2g}$ and $^3E_g$ ($^3T_{2g}$ in $O_h$) are expected to appear between 7500 and 12500 $cm^{-1}$.[42] Though the splitting between the two transitions is small (~1000 $cm^{-1}$) the spectrum can be deconvolved to show the $^3B_{2g}$ transition at 9550 $cm^{-1}$ and the $^3E_g$ peak at 10550 $cm^{-1}$ (Figure 5b). The two absorbances stemming from the $^3T_{1g}$ ($O_h$) state ($^3B_{1g}\rightarrow{}^3E_g$, $^3A_{2g}$) contain excessive overlap from other terms as well as charge transfer and $\pi\rightarrow\pi^*$ transitions and hence cannot be deconvolved. Thus the peak at 16420 $cm^{-1}$ is assigned to the combination of those two signals. The remaining spin-allowed and forbidden transitions are obscured by the other larger signals. For cobalt, six low energy spin allowed transitions are expected. However, none of these are sufficiently resolved in order to make definite assignments.

| Compound | Absorption Features [a] | | | | | | | | |
|---|---|---|---|---|---|---|---|---|---|
| | λ, $cm^{-1}$ (nm) | ε | Transition | λ, $cm^{-1}$ (nm) | ε | Transition | λ, $cm^{-1}$ (nm) | ε | Transition |
| **2** (Cu) | 14290 (700) | 28 | $^2B_{1g}\rightarrow{}^2B_{2g}$ [b] | 12990 (770) | 46 | $^2B_{1g}\rightarrow{}^2E_g$ [b] | 8670 (1154) | 189 | $^2B_{1g}\rightarrow{}^2A_{1g}$ |
| **3** (Ni) | - | - | - | 16420 (609) | 17 | "$O_h$ $T_{1g}$" $^3B_{1g}\rightarrow{}^3E_g$ + $^3B_{1g}\rightarrow{}^3A_{2g}$ | 10550 (948)<br>9550 (1047) | 31<br>31 | $^3B_{1g}\rightarrow{}^3B_{2g}$<br>$^3B_{1g}\rightarrow{}^3E_g$ ($^3T_{2g}$, $O_h$) |
| **4** (Co)[c] | 15530 (644) | 25 | - | - | - | - | 10830 (923) | 19 | - |

**Table 2.** Visible transitions observed in the transition metal complexes. [a] The spectrum that are not shown are included in the supplemental materials. [b] See previous section for discussion on these particular transitions. [c] Features are very broad and possibly encompass multiple transitions.

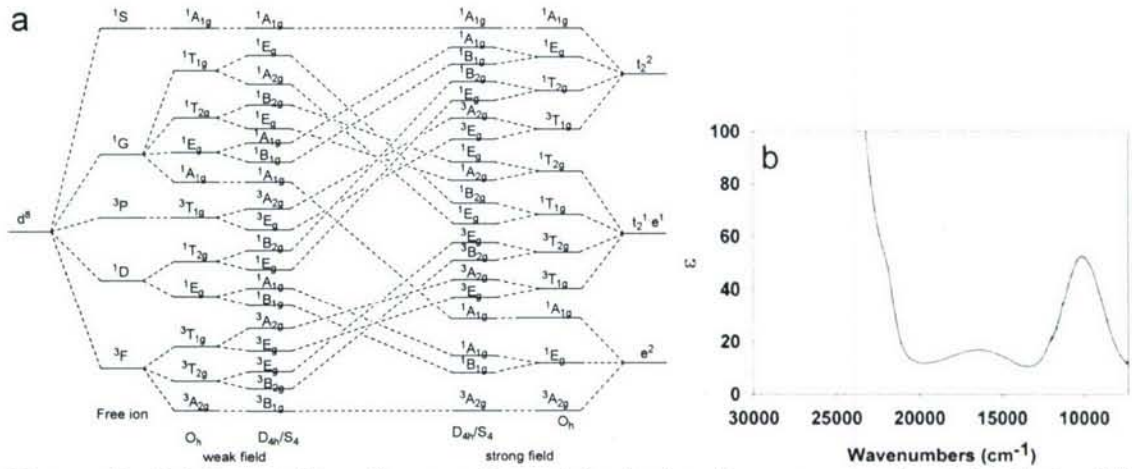


**Figure 5.** (a) Correlation diagram for octahedral and compressed octahedral splitting of $d^8$ configuration. Energy is not to scale. For more details on calculating energy transitions of nickel(II) in $D_{4h}$ fields see references.[43-45] (b) Visible spectrum of **3**.

Although the conjugated system is advantageous for transferring electrons throughout the molecule, the UV absorbance of the conjugated system makes assignment of the charge transfer signals problematic. The ligand $\pi \rightarrow \pi^*$ and charge transfer transitions are summarized in Figure 6 and Table 3.

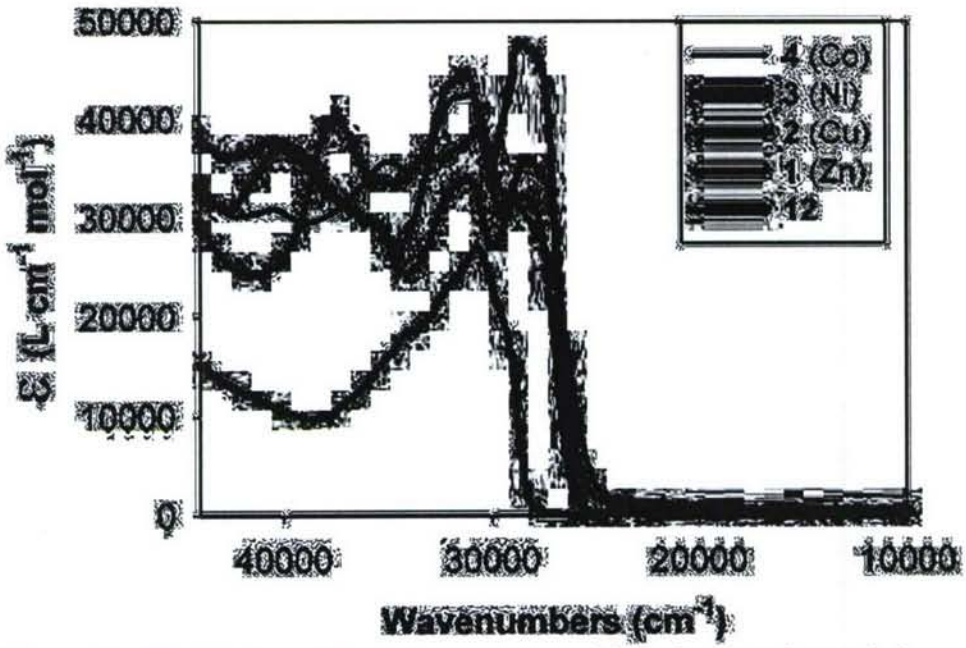


**Figure 6.** Charge transfer and $\pi \rightarrow \pi^*$ transitions in complexes **1-4**.

| Compound | Transitions $cm^{-1}$ (nm) | | | |
|---|---|---|---|---|
| **12** | - | - | 30680 (326) | - |
| **1** (Zn) | 40490 (247) | - | 31250 (320) | 28570 (350) |
| **2** (Cu) | 40160 (249) | - | 31150 (321) | 28650 (349) |

| | | | | |
|---|---|---|---|---|
| **3** (Ni) | 37590 (266) | 33110 (302) | 30770 (325) | 28330 (353) |
| **4** (Co) | 40490 (247) | 34970 (286) | 30160 (322) | - |

**Table 3.** The UV absorption band for compounds **1-4.**

*EPR*

The EPR spectrum of the copper compound allows for some confirmation of the predicted crystal field splitting. The measured g tensor can be predicted by the equation $g_{\alpha\beta} = g_e\delta_{\alpha\beta} + 2\lambda\sum_{n'}\frac{\langle n|L_\alpha|n'\rangle\langle n|L_\beta|n'\rangle}{E_n - E_{n'}}$,[46] where n is the orbital containing the unpaired spin, n' is the coupled orbital, L is the orbital angular momentum operator, $g_e$ is the g-factor for a free electron, λ is the spin orbit coupling constant and E represents the respective energy terms. If the unpaired electron lies in the $d_{z^2}$ orbital, the equation gives $g_{xx} = g_{yy} = g_e + 6\lambda/(E_{z^2} - E_{xz,yz})$ and $g_{zz} = g_e$. Hence an experimental value of $g_{zz}$ near that of a free electron (2.0023) and a larger $g_{xx,yy}$ is evidence for the predicted crystal field splitting.[47] The respective measured values for $g_\parallel$ ($g_{zz}$) and $g_\perp$ ($g_{xx}$,$g_{yy}$) are 2.020 and ~2.22 (the small amount of uncertainty in the latter being due to hyperfine splitting appearing near the inflection point). This confirms the unpaired electron lies in the $d_{z^2}$ orbital. The hyperfine splitting constant A is 200 gauss in the z direction. The hyperfine splitting constant is smaller than the linewidth for $g_{xx,yy}$.

By combining these results with the observed UV transitions, one can calculate λ' the observed spin-orbit coupling constant.[48,49] The ratio of λ'/λ provides a measure of the extent of covalency, or an indication as to the delocalization of the spin onto the ligand.[46,50] With $d_{xy}$ as the lowest lying d orbital ($d_{xy} \rightarrow d_{z^2}$ = 700 nm, see previous section), λ'/λ is equal to 0.57. This is quite low when compared to other simple copper(II) complexes.[51] It also provides experimental evidence that this compound contains a large amount of spin delocalization onto the ligands and has very good transport through the metal centers.

Such experimental evidence is welcome as we have previously shown unusually high Kondo temperatures in SMTs.[20,21] Kondo transport[15,16] (which can simplistically be thought of as electron transfer through unpaired spins) has a characteristic temperature that is exponentially sensitive to the coupling between the transition metal and the conduction electrons of the electrodes (through the ligands) onto which the molecule is assembled. The measured Kondo temperatures are comparable to those observed in scanning tunneling microscopy measurements of transition metals directly bonded to gold surfaces. This large extent of delocalization provides an experimental explanation for such a high source-spin-drain coupling.

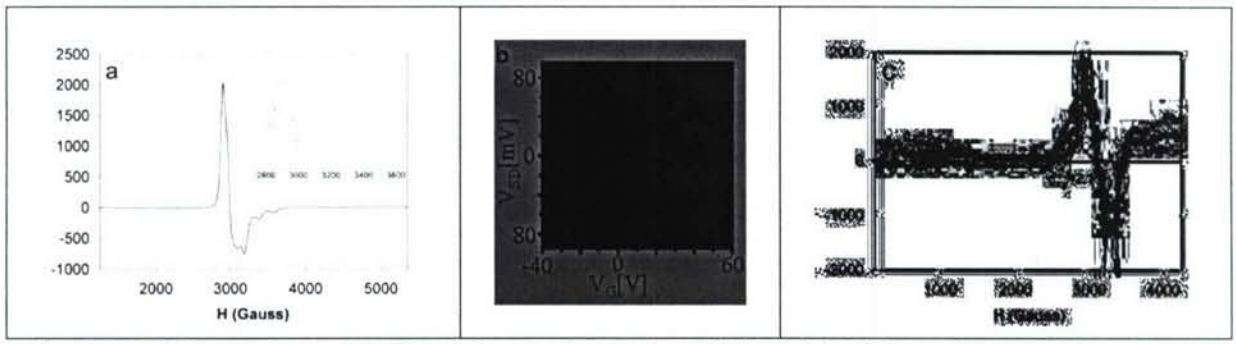


**Figure 7.** Magnetic properties of complexes **2** and **4**. (a) EPR spectrum of the copper complex **2**. Inlaid image is an enlarged portion of the spectrum. (b) A map of differential conductance ($dI_D/dV_{SD}$, black = 0, white = ($3 \times 10^{-5}$ siemens)) as a function of source-drain voltage ($V_{SD}$) and gate voltage ($V_G$) in a single-molecule transistor incorporating the complex **4**. The bright feature in conductance near $V_{SD} = 0$ is the Kondo resonance, which appears below $T=T_K$, and has a low-temperature width proportional to $T_K$.[20] (c) EPR spectrum of the cobalt complex **4** at various receiver gains.

For the cobalt species (Figure 7c) we observe large magnetic anisotropy consistent with that seen in literature for cobalt(II) where S=3/2.[52] The large g factor (4.3) becomes anisotropic when the octahedral symmetry is distorted by trigonal[53] or tetragonal distortion.[54] This results in additional terms along the diagonal of the energy matrix which supplement spin-orbit coupling. Further discussion of this phenomenon can be found elsewhere.[40,52,55] In our system $g_\perp$ was observed to be 2.1 with $g_\parallel$ equal to 8.27. The hyperfine splitting constant A is 135 gauss in the z direction.

*Magnetic Susceptibility*

The magnetic susceptibility of compounds **1-5** were examined by SQUID. Analysis of complexes **1-3** was straightforward. As expected, the zinc(II) complex **1** has no unpaired spins and is diamagnetic with a susceptibility of $-4.68 \times 10^{-4}$ emu/mol. The copper(II) complex **2** with a $3d^9$ configuration behaves like a well defined spin 1/2 paramagnetic compound (Figure 8a,b). Low field data gives a magnetic susceptibility of 1.76 BM, similar to the 1.73 BM expected for a spin ½ compound with no orbital contributions. The high field data can be fit with a with a Brillouin function with j = 0.5 and g = 2.02. The nickel(II) species **3** is similarly straightforward at high temperatures with a effective magnetic moment of 4.3 BM.

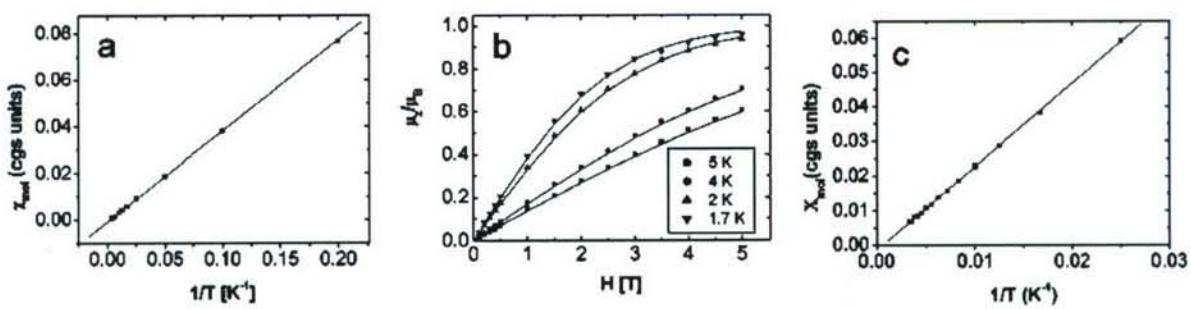

**Figure 8.** Magnetization data for **2** and **3**. (a) SQUID low field data for copper compound **2**. (b) High field data for compound **2**. (c) SQUID low field data for nickel compound **3**.

The behavior of the cobalt(II) complex **4** was much more complex. We discovered from measurements on powders that this material's susceptibility is highly anisotropic; as a result we were forced to collect data from a particularly large single crystal (2.6 mg). The single crystal data indicates that the cobalt complex is strongly paramagnetic along one axis and weakly paramagnetic along the other two. According to low-field dc susceptibility measurements, the weakly paramagnetic axes have an effective magnetic moment of 2.6 BM and the strongly paramagnetic axis give an effective magnetic moment of 9.2 BM. The crystallographic axes are coincident with the molecular axes

The magnetization data on the iron(II) complex **5** also yielded interesting information. While the data above ~6 K is highly suggestive of a system with four unpaired spins (with an effective magnetic moment of 5.9 BM), it is clear that the magnetization data plotted vs. H/T below 6 K fall on different curves (Figure 9). This suggests that zero field splitting plays a significant role in the magnetic properties of the iron complex. Alternatively, it is possible that the low temperature data hint at the onset of a transition to a low spin state.

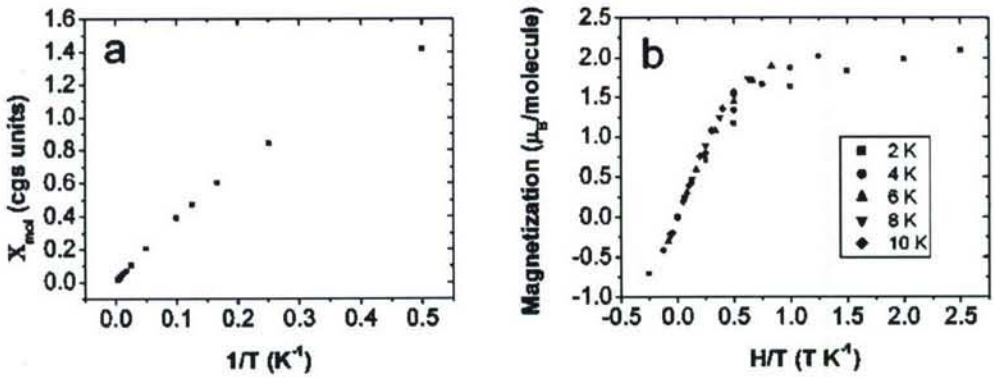


**Figure 9**. Magnetization data of for the iron complex **5**. (a) SQUID low field data for **5**. (b) SQUID high field data for **5**.

*CV*

| *Compound* | *Metal Reduction* | *Voltage (V)* | *Metal Oxidation* | *Voltage (V)* |
|---|---|---|---|---|
| **2** | $Cu^{II} \rightarrow Cu^{I}$ | -0.80 | $Cu^{I} \rightarrow Cu^{II}$ | -0.66 |
| **3** | $Ni^{III} \rightarrow Ni^{II}$ | 0.77 | $Ni^{II} \rightarrow Ni^{III}$ | 0.87 |
| **4** | $Co^{III} \rightarrow Co^{II}$ | -0.012 | $Co^{II} \rightarrow Co^{III}$ | 0.14 |
| **10** | $Co^{III} \rightarrow Co^{II}$ | -0.42 | $Co^{II} \rightarrow Co^{III}$ | -0.30 |
| **5** | $Fe^{III} \rightarrow Fe^{II}$ | 0.20 | $Fe^{II} \rightarrow Fe^{III}$ | 0.39 |

**Table 4.** The reversible reductions/oxidation of the metal centers. The oxidations reductions were performed on the metal complexes **1-5**, **10** (1 mM) in THF with 0.1 M

$TBABF_4$ as the supporting electrolyte. The scan rate for all of the redox potentials was 20 mV/s with the exception of **5** which was at 600 mV/s.

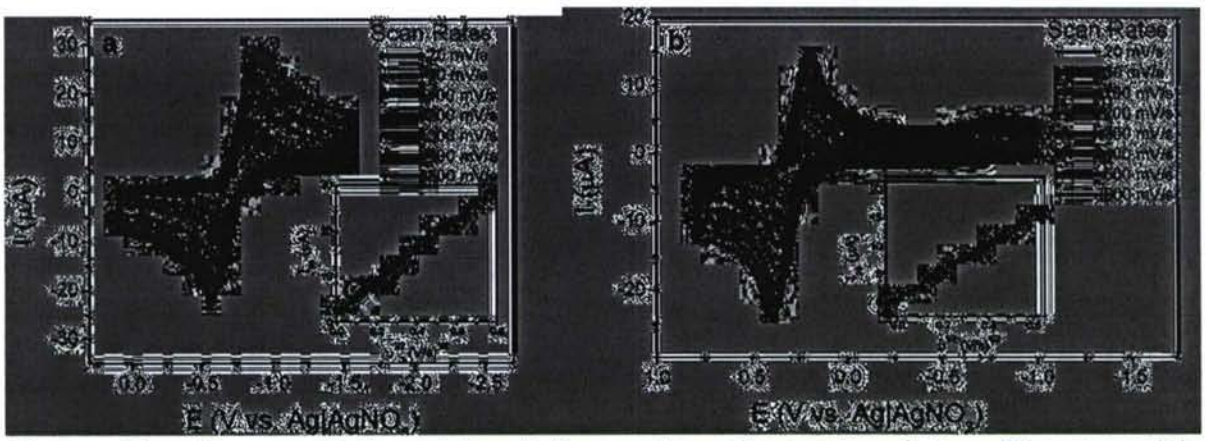


**Figure 10.** Representative plots of the cyclic voltammetry data. The reversible reduction/oxidation of (a) copper complex **2** and (b) the iron complex **5**. The linear relationship between the oxidation peak currents and square root of scan rates, as shown in the insets, indicates a diffusion-controlled redox process.

From cyclic voltammetry we can see that all molecules are overall neutral with a metal(II) center (Table 4, Figure 10). As the potential is increased both nickel(II) **3** and iron(II) **5** complexes undergo a reversible oxidation to nickel(III) and iron(III). This reversible oxidation and reduction occurs at 0.87 and 0.77 V (vs. $Ag|AgNO_3$, 20 mV/s) for nickel and 0.393 to 0.197 for iron (at 600 mV/s). It is worth noting that there is an extra feature at -0.69 V for iron. None of the other compounds (**1-4**) demonstrated this feature. When we further investigated this phenomenon we saw that it was not present when scanning from -0.1 V to -1.0 V but was present when the scan was cycled from -1.0 V to 0.75 V and then back to -1.0 (Figure 11a). We surmise that this phenomenon is responsible for the reduction current peak ($I_{pc}$) always being smaller than the oxidation current peak ($I_{pa}$). Because the ratio of these two peaks approach unity as the scan rate is increased (Figure 11b) it is natural to suggest that this is a rearrangement phenomenon (be it ligand association or dissociation), which is consistent with the lack of stability for **5** as mentioned earlier.

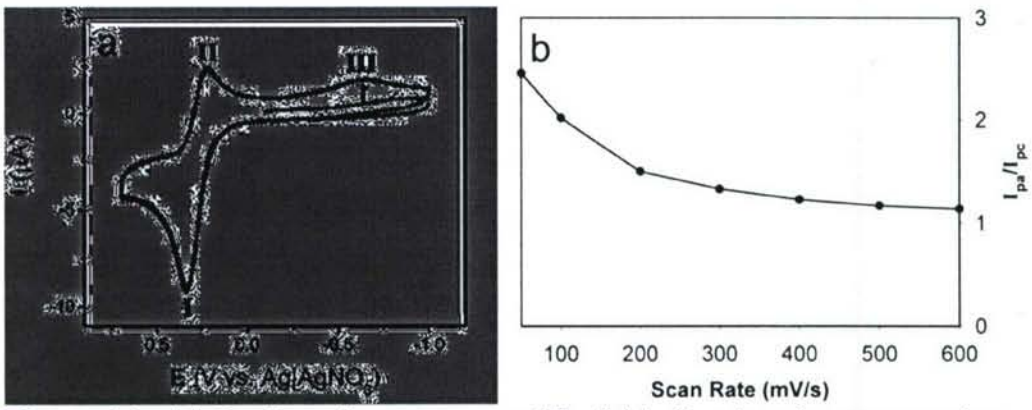


**Figure 11.** (a) Cyclic voltammagram of **5**. (b) $I_{pa}/I_{pc}$ at various scan rates.

The CV of the cobalt compound **4** shows the reduction and oxidation at -0.01 and 0.14 V respectively. It is useful to compare its redox potential with that of simple SCN-free cobalt compound **10**, which has its oxidation/reduction at -0.42 and -0.30 V, respectively. From such comparison we see that the thiocyanate moiety has the effect of decreasing the reduction potential of the metal (-0.38 V for **10**, -0.01 V for **4**), apparently by reducing the electron density available in the pyrrole ring, and in turn the metal center. This is further supported by theoretical modeling of the compounds which shows a decrease in the electron density of the pyrrole ring (illustrated in Figure 12) when the thiocyanate moieties are on the pyrrole ring.

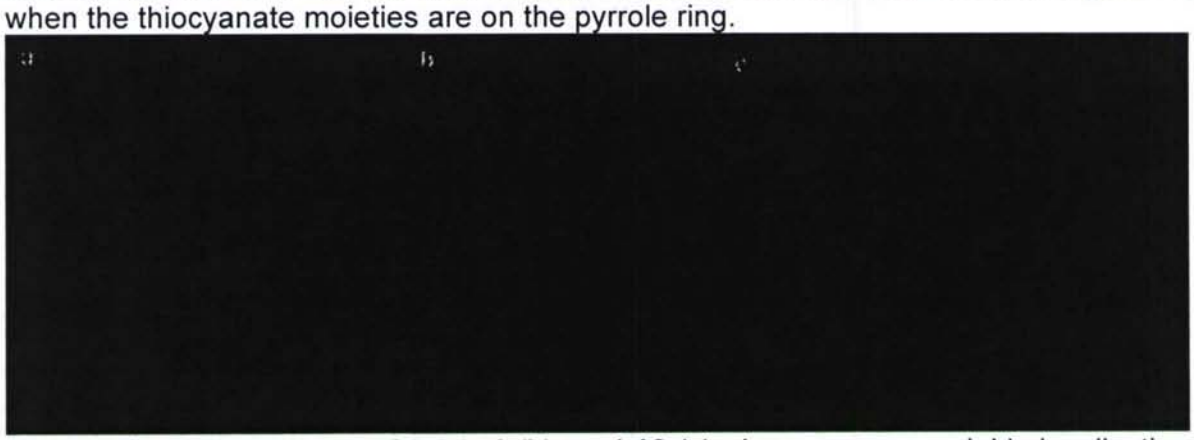

**Figure 12.** Potential map of **9** (a), **1** (b), and **12** (c). Images are overlaid visualizations of electron density and potential maps. The calculation was performed using the Gaussian 98 software suite[56] with SDD[57,58]basis set on the X-ray crystal structure data. The output was visualized with gopenmol.[59,60] Red denotes the most electron-rich areas, blue, the most electron-deficient.

Neither the zinc compound **1** or the copper compound **2** are readily oxidized to the metal(III) oxidation state. With the copper compound **2**, the lowest energy transition is to the metal(I) state. This reduction and oxidation occur at -0.80 and -0.66 V. The zinc compound **1**, as expected, shows no oxidation or reduction within a window from +1.0 to -1.6 V.

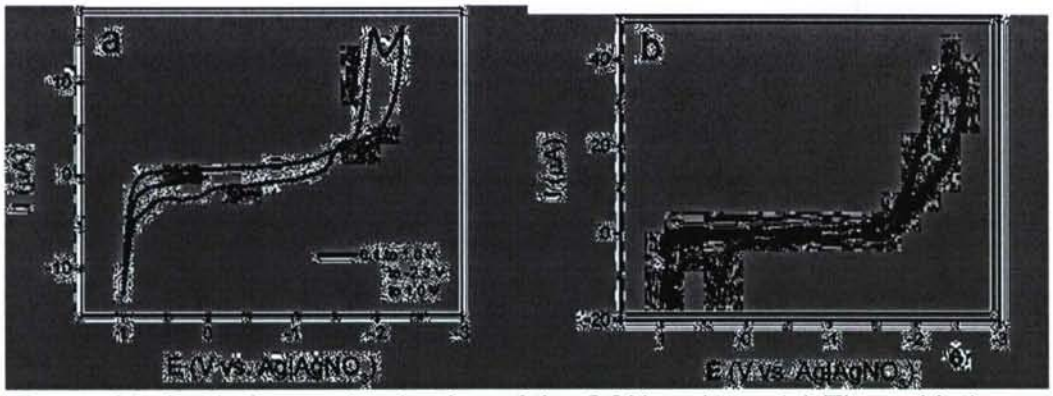

**Figure 13.** Oxidation and reduction of the SCN moiety. (a) The oxidation and reduction of the free ligand **12.** (b) The oxidation and reduction of **1**.

The zinc compound **1** does, however, show is the oxidation and reduction of the thiocyanate group (Figure 13). In agreement with recently published data,[61,62] we clearly see the thiocyanate reduction to thiolate at -2.0 to -2.2 V for **1** (zinc), **3** (nickel), **4** (cobalt), and **12**. The corresponding oxidation features (ca 0.3 V) are attributed to the formation of disulfide bonds. This data shows the sensitivity of the reduction to the electron density in the adjacent ring. As a general trend, when the ring is electron deficient, the reduction occurs at a more positive voltage. In our experiments the electron poor ligand **12** shows the reduction at -1.96 V. If this data is then compared to the zinc, nickel, and cobalt complexes (-2.2, -2.08 V and -2.1 V, respectively) we observe this same trend. When the ligand (in the complex) is electron-deficient due to a high degree of covalency with the metal core, the thiocyanate reduction occurs at a more positive potential. This is also supported by theoretical calculations (Table 5) which show this same relationship. Thus Table 5 can be used to map the trend of the degree of covalency of the metal.

| Metal | Calculated Charge on the Metal | Average Calculated Charge on Pyrrole Nitrogen | SCN reduction potential (V) |
|---|---|---|---|
| None | 0.43 | -0.59 | -1.96 |
| Co | 1.68 | -0.65 | ~2.1 |
| Ni | 1.79 | -0.69 | -2.08 |
| Zn | 1.87 | -0.74 | -2.2 |

**Table 5.** Correlation between electron charge on the metal centers and reduction of the SCN moiety. Calculations were performed with the Gaussian 98 suite of software.[56] Hartree-Fock calculations were preformed with the SDD basis set.[57,58]

*Infrared 4000-400 $cm^{-1}$ (2500-25000 nm)*

Several IR assignments can be made unambiguously and can be useful in corroborating the relative electron densities of various parts of the ligand. The most obvious stretch is the $\nu$(CN) which occurs at ~2150 $cm^{-1}$. The signal at ~680-690 $cm^{-1}$ can also be attributed to the thiocyanate functionality. The stretches at ~1590 are $\nu$(C=C) and $\nu$(C=N). A stretch at 1583 $cm^{-1}$ is generally attributed to pyridine C=C and C=N stretches, it is well known that this stretch shifts to higher wavenumbers for

pyridine complexation.[63] In our case the shift is not as large due to the longer than usual pyridine-metal bond length. Most of the other peaks vary too much in location or intensity to make an assignment. The stretches falling between 1520-1430 $cm^{-1}$ belong to the ring breathing ($\nu$(C=C) and $\nu$(C=N)), with the two stretches at 1460-1430 likely belonging to the pyridine.

These IR assignments can be useful in the discussion of the electronic effect of the metal centers on the SCN reduction. Should the arguments regarding the SCN reduction potentials and their relationship with the delocalization of ligand electrons onto the metal (made in the previous section) be valid, we would also expect to see corresponding changes in the SCN frequencies. The trend is obvious in the case of the electron dependent CN stretch (Table 6).

| Compound # | **12** | **4** | **3** | **5** | **2** | **1** |
|---|---|---|---|---|---|---|
| Metal | None | Co | Ni | Fe | Cu | Zn |
| SCN Reduction | -1.96 | ~-2.0 | -2.08 | - | - | -2.2 |
| $\nu$(CN), $cm^{-1}$ | 2152.0 | 2150.1 | [(a)] | 2149.1 | 2148.9 | 2148.7 |
| $\nu$(C-S), $cm^{-1}$ | 733.9 | 743.8 | 744.1 | 743.0 | 743.7 | 743.3 |
| $\nu$(C-S), $cm^{-1}$ | 686.6 | 696.5 | 699.3 | 698.3 | 698.5 | 699.0 |

**Table 6**. Thiocyanate infrared stretches for the metal complexes **1-5** and the free ligand **12**. [(a)] Two separate peaks appear for the nickel compound **3** in the thiocyanate region as a result of a slight difference in bond lengths of one of the thiocyanates.

**Surface Characterization**

Surface characterization of the molecular assemblies focuses on analytically determining which, if any, aspects of the molecule may have changed during the assembly procedure. Though thiocyanates are known to prevent disulfide polymerization,[22] and the rigidness and orthogonality of the ligands prevent both ligands from binding to gold at the same time (Figure 14), confirmation was needed. We also examined the molecules for ligand loss, metal oxidation/reduction, or substituent decomposition.

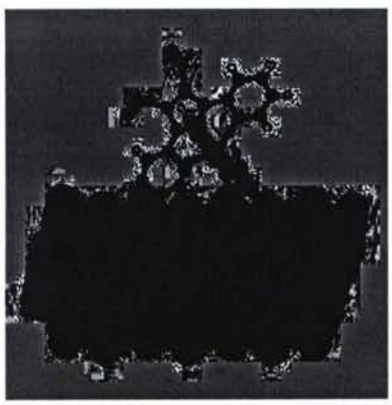

**Figure 14.** Modeling of the cobalt containing molecule **4** assembled on a gold (111) surface.

*X-ray photoelectron spectroscopy (XPS)*

XPS is a powerful tool available for discerning the state of the molecule on the surface. By comparing the spectral data of the powder sample to that of the assembled molecule, we can observe the bonding of the sulfurs, and any change in the oxidation state of the metal center, as well as other changes that may occur upon assembly.

Initially, we sought confirmation that the molecules were covalently bound to the surface. An advantage of the thiocyanate assemblies is that thiolates (Au-S) generated during the assembly have substantially more electron density than the thiocyanates (-SCN) and can be distinguished easily by XPS (Figure 15a,b).[22,23] Thus these two peaks are an indication that one set of sulfurs are bound to gold, the other to CN. All compounds showed similar sulfur regions. As a general trend, all thiolate regions were of slightly larger intensity than the thiocyanate region. A possible reason for this discrepancy is that at several areas on the substrate, surface roughness (which is closer to curvature on the atomic scale) may allow three or four sulfurs to reach the surface. When this is averaged out over all the surfaces, we would expect to see a ratio of thiolate to thiocyanate that is larger than 1:1. However, when assemblies were performed on gold on the flatter mica surface, there was no change in the S-Au to S-CN ratio from assemblies done on gold-silicon surfaces. Another possibility, disproportionation, is ruled out (vide infra). X-ray meditated decomposition of the thiocyanate can be ruled out as multiple scans in the same region show no difference in intensity. We are left to conclude that the difference is due to a combination of a slight difference in the efficiency of the photoelecton process and / or a charging effect. Charging can retard the formation of photoelectrons. A difference in the effectiveness of the neutralizer on the gold thiolates vs. the thiocyanates will in turn cause a difference in the measured intensity by XPS. Since the difference appears consistently from sample to sample, such a mechanism seems likely.

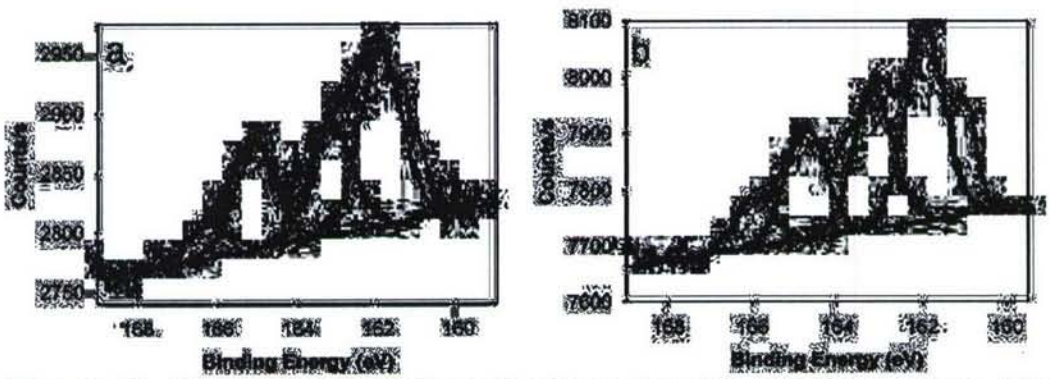


**Figure 15.** Deconvolution of the sulfur 2p region of the XPS spectrum. The left pair of peaks in each figure are due to the thiocyanates (-SCN), the right pair from the thiolates (Au-S). (a) Deconvolution of the S 2p region in the surface-assembled sample of **4**. (b) Deconvolution of the S 2p region in the surface-assembled sample of **2.**

XPS allows the examinations of the surface assembly for other signs of change in the molecule. Large changes in binding energy of the elements would be indicative of a change in oxidation state or bonding motif. Table 7 and Figure 16 summarize the binding energies of each element of the complex showing both the powder spectrum

and surface assembly. No substantial changes in binding energies were seen, indicating the assembled molecule was similar to the powder form except for the fact that two of the thiocyanates had been converted to thiolates. The small shift in both nitrogen and cobalt energies can be attributed to the difference in electron density of the ligand when the electron withdrawing thiocyanates are converted to electron rich thiolates. According to atomic concentration calculations performed using the PHI Multipak software, the ratio (corrected for the atomic sensitivity factors of each respective element) of cobalt to S in the crystalline powder sample of **4** matched the ratio found in the surface-assembled sample. This indicates that the metal complex has not disproportionated or decayed and is most likely intact on the surface.

| Spectral component | Surface spectrum binding energy (eV) | | Powder spectrum binding energy (eV) |
|---|---|---|---|
| S $2p^{3/2}$ | 161.9 (Au-S) | 165.0 (-SCN) | 164.8 |
| S $2p^{1/2}$ | 163.2 (Au-S) | 166.4 (-SCN) | 166.2 |
| Co $2p^{3/2}$ | 781.6 | | 780.4 |
| Co $2p^{1/2}$ | 796.5 | | 796.3 |
| N 1s | 399.3 | | 398.6 |

**Table 7**. Comparison of the XPS binding energies of the powdered and assembled forms of **4**.

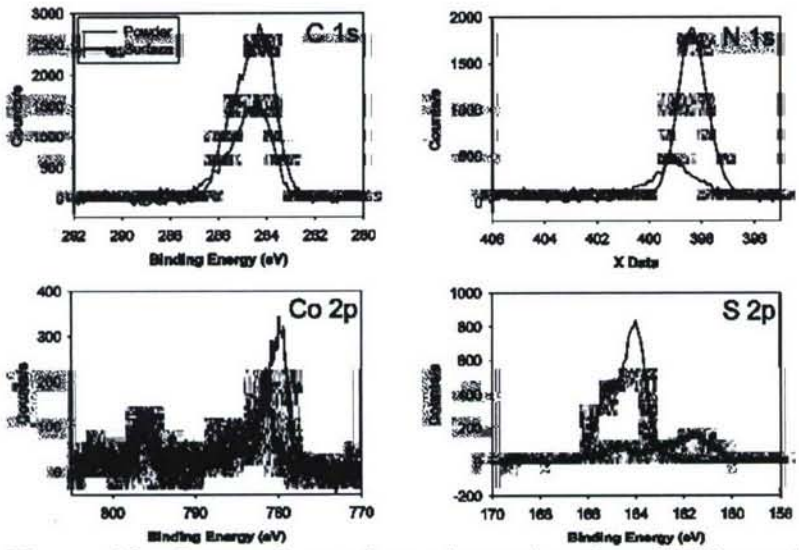


**Figure 16**. Comparison of powder and surface XPS spectra of **4**. Results are representative of the data for **1-4**.

*Ellipsometry*

Ellipsometry was carried out on the self-assembled monolayers (SAMs). Due to the bulky nature of the molecules we did not expect the packing to approach the theoretical height of the molecule. For a layer of bulky molecules on the surface we would expect a thickness of about 11-12 Å[64] while for a well-packed monolayer the thickness would be 14 Å. Ellipsometric values lie in-between these two, but do not give

a definitive indication due to the error in the measurement. Thiocyanate assembly has been previously shown to prevent multilayers,[22] and ellipsometry confirms this for these complexes.

| Molecule | Measured Thickness (Å) |
|---|---|
| Zn (**1**) | 13.5 |
| Ni (**3**) | 10.5 |
| Co (**4**) | 12.8 |

**Table 8.** The film thickness (±10%) for assemblies of **1-4**. The calculated height for surface bound metal complex is 14 Å.

*Infrared Reflection Spectroscopy Measurements*

IR reflection spectroscopy was used for a secondary confirmation of the presence of the thiocyanate after assembly. Both the nickel and cobalt complexes were examined. In both cases the thiocyanate was clearly visibly by IR and had nearly an identical stretch to that of the powder. The surface stretch had shifted ~1 $cm^{-1}$ higher but appear at similar values to the powder spectrum (Table 9).

| Compound | $\nu_1$(CN) (Powder) $cm^{-}$ | $\nu_1$(CN) (Surface) $cm^{-}$ |
|---|---|---|
| **3** | 2155.6, 2146.8 | 2156.5, 2147.1 |
| **4** | 2150.1 | 2151.7 |

**Table 9.** Stretching frequencies of the CN triple bond.

**SMT Testing**

With assembly of the molecules on the gold surface established, we were able examine these features in SMTs. For these devices a small percentage of the chips produced contained a small witness pad where molecular assembly was examined. In all cases, the assembly on the witness pad mirrored that seen for bulk substrates.

SMT devices consisted of thin metal constrictions (defined by electron beam lithography and e-beam evaporation) on silicon oxide, which were then broken by electromigration. The underlying silicon behaves as a gate. A percentage of the devices (~15%) demonstrated gate dependent behavior consistent with molecular devices. We have statistically examined this molecular system[19] along with appropriate alkane thiol controls. In many devices we observed conductance features characteristic of the Kondo effect, a coherent many-body state comprising an unpaired spin on the molecule coupled by exchange to the conduction electrons of the leads. Kondo temperatures in excess of 50 K were found, comparable to those in a purely metallic system. In addition to the Kondo resonance some of these SMTs exhibit inelastic cotunneling features that correspond energetically to vibrational excitations of the molecule, as determined by Raman and infrared spectroscopy.[13] This is a form of inelastic electron tunneling spectroscopy of single molecules, with transistor geometry allowing in situ tuning of the electronic states via a gate electrode. The interested reader can further examine these results in their entirety in the aforementioned references.

## Conclusions

We have shown a simple and efficient method for the synthesis of the transition metal complexes **1-5**. Characterization of these compounds allows us to predict and explain many of the electronic properties of these molecules in SMTs. The complexes have a high degree of covalency between the metal core and ligands, explaining the origin of high Kondo temperatures in SMTs. Assembly of the molecules on gold gives a thickness consistent with what is expected for a loosely packed layer of bulky molecules. Other surface characterization (XPS, surface IR) show species pre- and post- assembly that are virtually identical except for the two thiocyanates that have been converted to thiolates during assembly. Lastly, all tests of the molecules on witness pads for SMT devices display the same properties as those on a bulk substrate.

## References


1. Reed, M. A.; Zhou, C.; Muller, C. J.; Burgin, T. P.; Tour, J. M. *Science* **1997,** 278, 252-254.
2. Bumm, L. A.; Arnold, J. J.; Cygan, M. T.; Dunbar, T. D.; Burgin, T. P.; L., I. J.; Allara, D. L.; Tour, J. M.; Weiss, P. S. *Science* **1996,** 271, 1705-1707.
3. Dorogi, M.; Gomez, J.; Osifchin, R.; Andres, R. P.; Reifenberger, R. *Phys. Rev. B: Condes. Matter.* **1995,** 52, 9071-9077.
4. Andres, R. P.; Bein, T.; Drorogi, M.; Feng, S.; Henderson, J. I.; Kubiak, C. P.; Mahoney, W.; Osifchin, R. G.; Reifenberger, R. *Science* **1996,** 272, 1323-1325.
5. Joachim, C.; Gimzewski, J. K. *Europhys. Lett.* **1995,** 30, 409-414.
6. Joachim, C.; Gimzewski, J. K.; Schlittler, R. R. *Phys. Rev. Lett.* **1995,** 74, 2102-2105.
7. Fischer, C. M.; M., B.; Roth, S.; Klitzing, K. v. *Appl. Phys. Lett.* **1995,** 66, 3331-3333.
8. Park, J.; Pasupathy, A. N.; Goldsmith, J. I.; Chang, C.; Yaish, Y.; Petta, J. R.; Rinkoski, M.; Sethna, J. P.; Abruna, H. D.; McEuen, P. L.; Ralph, D. C. *Nature* **2002,** 417, 722-725.
9. Liang, W.; Shores, M. P.; Bockrath, M.; Long, J. R.; Park, H. *Nature* **2002,** 417, (13), 725-729.
10. Yu, L. H.; Natelson, D. *Nano Lett.* **2004,** 4, 79-83.
11. Kushmerick, J. G.; Lazorcik, J.; Patterson, C. H.; Shashidhar, R. *Nano Lett.* **2004,** 4, 639-642.
12. Wang, W.; Lee, T.; Kretzschmar, I.; Reed, M. A. *Nano Lett.* **2004,** 4, 643-646.
13. Yu, L. H.; Keane, Z. K.; Ciszek, J. W.; Cheng, L.; Stewart, M. P.; Tour, J. M.; Natelson, D. *Phys. Rev. Lett.* **2004,** 93, 266802.
14. Stipe, B. C.; Rezaei, M. A.; Ho, W. *Science* **1998,** 280, 1732-1735.
15. Kondo, J. *Prog. Theor. Phys.* **1964,** 32, 37-49.
16. Anderson, P. W. *Phys. Rev.* **1961,** 124, 41-53.
17. Jaklevic, R. C.; Lambe, J. *Phys. Rev. Lett.* **1966,** 17, 1139-1140.
18. Adkins, C. J.; Phillips, W. A. *J. Phys. C: Solid State Phys.* **1985,** 18, 1313-1346.
19. Natelson, D.; Yu, L. H.; Ciszek, J. W.; Keane, Z. K.; Tour, J. M. *J. Chem. Phys.,* submitted for publication, **2005**.
20. Yu, L. H.; Keane, Z. K.; Ciszek, J. W.; Cheng, L.; Tour, J. M.; Baruah, T.; Pederson, M. R.; Natelson, D., *Phys. Rev. Lett.,* submitted for publication, **2005**.

21. Pederson, M. R.; Baruah, T. Unpublished work, 2005.
22. Ciszek, J. W.; Stewart, M. P.; Tour, J. M. *J. Am. Chem. Soc.* **2004**, 13172-13173.
23. Ciszek, J. W.; Tour, J. M. *Chem. Mater.,* submitted for publication, **2005**.
24. Bain, C. D.; Troughton, E. B.; Tao, Y.-T.; Evall, J.; Whitesides, G. M.; Nuzzo, R. G. *J. Am. Chem. Soc.* **1989,** 111, 321-335.
25. Tour, J. M.; Jones, L., II; Pearson, D. L.; Lamba, J. S.; Burgin, T. P.; Whitesides, G. M.; Allara, D. L.; Parikh, A. N.; Atre, S. V. *J. Am. Chem. Soc.* **1995,** 117, 9529-9534.
26. Stapleton, J. J.; Harder, P.; Daniel, T. A.; Reinard, M. D.; Yao, Y.; Price, D. W.; Tour, J. M.; Allara, D. L. *Langmuir* **2003,** 19, 8245-8255.
27. Jones, A. R.; Karatza, M.; Voro, T. N.; Civcir, P. U.; Franck, A.; Ozturk, O.; Seaman, J. P.; Whitmore, A. P.; Williamson, D. J. *Tetrahedron* **1996,** 52, 8707-8724.
28. Hein, B.; Beierlein, U. *Pharmazeutische Zentralhalle* **1957,** 96, 401-421.
29. Schindlbauer, H. *Monatsh. Chem.* **1968,** 99, 1799-1807.
30. Owsley, D. C.; Nelke, J. M.; Bloomfield, J. J. *J. Org. Chem.* **1973,** 38, 901-903.
31. The design is such that there is a continuous conducting pi system throughout the molecule except were the electrons are forced to travel through the metal atom. The alligator clips must be in a position such that each metal lead in a SMT attaches to only one ligand and thus electrons travel from lead to lead through the metal center as opposed to from end to end of one ligand.
32. Ulman, A. *Chem. Rev.* **1996,** 96, 1533-1554.
33. Tour, J. M., *Molecular Electronic: Commercial Insights, Chemistry, Devices, Architecture and Programming*. World Scientific: River Edge, New Jersey, 2003.
34. Halcrow, M. A. *J. Chem. Soc., Dalton Trans.* **2003**, 4375-4384.
35. Murphy, A.; Mullane, J.; Hathaway, B. *Inorg. Nucl. Chem. Lett.* **1980,** 16, 129-134.
36. Figgis, B. N., *Introduction to Ligand Fields*. John Wiley & Sons: New York, 1966.
37. Procter, I. M.; Hathaway, B. J.; Nicholls, P. *J. Chem. Soc. A* **1968**, 1678-1684.
38. Hathaway, B. J.; Bew, M. J.; Billing, D. E. *J. Chem. Soc. A* **1970**, 1090-1095.
39. Stephens, F. S. *J. Chem. Soc. A.* **1969**, 883-890.
40. Pilbrow, J. R., *Transition Ion Electron Paramagnetic Resonance*. Clarendon Press: Oxford, 1990.
41. Ferguson, J.; Wood, D. L.; Knox, K. *J. Chem. Phys.* **1963,** 39, 881-889.
42. Lever, A. B. P.; Walker, I. M.; McCarthy, P. J. *Inorg. Chim. Acta* **1980,** 39, 81-90.
43. Schreiner, A. F.; Hamm, D. J. *Inorg. Chem.* **1973,** 9, 2037-2048.
44. Maki, G. *J. Chem. Phys.* **1958,** 28, 651-662.
45. Rowley, D. A.; Drago, R. S. *Inorg. Chem.* **1967,** 6, 1092-1096.
46. Atherton, N. M., *Principles of Electron Spin Resonance*. Horwood, PTR Prentice Hall: New York, 1993.
47. Palmer, G. *Biochem. Soc. Trans.* **1985,** 13, 548-560.
48. Dunn, T. M. *J. Chem. Soc.* **1959**, 623-627.
49. Owen, J. *Proc. R. Soc. London Ser A.* **1955,** 227, 183-200.
50. Cotton, F. A.; Goodgame, D. M. L.; Goodgame, M. *J. Am. Chem. Soc.* **1961,** 83, 4690-4699.
51. Hathaway, B. J.; Billing, D. E.; Nicholls, P.; Procter, I. M. *J. Chem. Soc. A* **1969**, 319-325.
52. Abragam, A.; Pryce, M. H. L. *Proc. R. Soc. London Ser A.* **1951,** 206, 173-191.

53. Jesson, J. P. *J. Chem. Phys.* **1966,** 45, 1049-1056.
54. Bleaney, B.; Ingram, D. J. E. *Proc. R. Soc. A.* **1951,** 208, 143-158.
55. Abragam, A.; Bleaney, B., *Electron Paramagnetic Resonance of Transition Ions.* Clarendon Press: Oxford, 1970.
56. Frisch, M. J.. et. al. *Gaussian 98*, Revision A.11; Gaussian Inc.: Pittsburgh, PA, 2001.
57. Dunning, T. H. J.; Hay, P. J., *Modern Theoretical Chemistry*. Plenum Press: New York, 1977; Vol. 3.
58. Igel-Mann, G.; Stoll, H.; Preuss, H. *Mol. Phys.* **1988,** 65, 1321-1328.
59. Laaksonen, L. *J. Mol. Graph.* **1992,** 10, 33-34.
60. Bergman, D. L.; Laaksonen, L.; Laaksonen, A. *J. Mol. Graph. Model.* **1997,** 15, 301-306.
61. Houmam, A.; Hamed, E. M.; Hapiot, P.; Motto, J. M.; Schwan, A. L. *J. Am. Chem. Soc.* **2003,** 125, 12676-12677.
62. Houmam, A.; Hamed, E. M.; Still, I. W. J. *J. Am. Chem. Soc.* **2003,** 125, 7258-7265.
63. Gupta, R. R., *Physical Methods in Heterocyclic Chemistry*. Wiley-Interscience: New York, 1984.
64. Wo, C.-G.; Chiang, S.-C.; Wu, C.-H. *Langmuir* **2002,** 18, 7473-7481.

## Mechanistic Implications of the Assembly of Organic Thiocyanates on Precious Metals

Thiocyanate assembly is shown to be an effective method for assembling thiolate structures on platinum, silver, and gold. The assemblies were studied by infrared reflection spectroscopy and X-ray photoelectron spectroscopy (XPS). Two cyanide species were identified on the surfaces: the first corresponding to adsorbed cyanide and the second to a form commonly seen as an intermediate during cyanide etching of metals. The presence of the second species supports the theory that cyanide is leaving the surface as $M(CN)_x$, resulting in a thiolate monolayer. Comparison of thiocyanate assemblies on evaporated gold and silver to those on template-stripped gold demonstrates the integral role of surface morphology in the expulsion of $(CN)_{ads}$ from the surface of the metals.

### Introduction

The assembly of organic thiocyanates has recently been demonstrated on evaporated gold surfaces.[1] This new process for the formation of self-assembled monolayers has the advantage that it does not require exogenous deprotection additives nor an oxygen-free system for assembly. In addition, thiocyanates are more stable than traditional thiols; this is especially important for aromatic variants where the thiol oxidative instability rapidly leads to disulfide formation and often subsequent precipitation. The thiocyanate assembly on gold also gives the same thiolate bonding structure as thiol assemblies with no sign of cyanide contamination. The hypothesized mechanism is a surface mediated reduction of the thiocyanate, with the cyanide leaving as $[Au(CN)_2]^-$ (Figure 1).

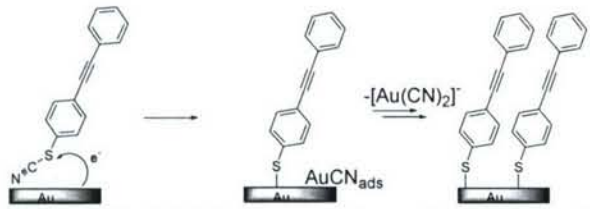


**Figure 1.** Initial proposed mechanism for thiocyanate assembly.

At the time of our report,[1] little evidence was available for the hypothesized mechanism. Part of the difficulty in obtaining such confirmation is the nature of the $Au(CN)_{ads}$ species since it is rarely present in large concentrations, and isolating the trace $[Au(CN)_2]^-$ generated by the reaction is difficult. This is further compounded by the dearth of literature concerning cyanide related adsorbates on gold,[2-5] which is due in part to the propensity of such solutions to etch the surface. Therefore, for further clarification of the mechanistic aspects of thiocyanate assembly, we have performed assemblies on platinum and silver. The differences between substrates and their respective thiolate monolayers allow us to make more definitive statements about the assembly mechanism. Silver differs from gold in many properties including work function,[6] surface energy,[7] surface energy heterogeneity[8] and monolayer packing density.[9] For platinum, the well-characterized $Pt(CN)_{ads}$ state gives us ample opportunity to analyze the different adsorbed states, which will allow for parallels to the $Au(CN)_{ads}$ state. The free thiol assemblies are known for these precious metals,[10-13] and both silver and platinum assemblies occur in a manner similar to that of the gold-thiol assemblies with the caveat that silver and platinum are prone to surface oxidation, which interferes with the assemblies. Thus care must be taken to exclude oxygen during the assembly processes on silver and platinum. Though this mitigates some of the advantages of the thiocyanate system, the insight garnered from these assemblies is required to gain a better understanding of the mechanism of thiocyanate assembly on gold.

## Experimental

**Materials.** 1-Dodecanethiol and 1-octanethiol were obtained from Aldrich. The synthesis of $C_8H_{17}SCN$ can be found in the supporting information. All other compounds were prepared as described previously.[1] Ethanol (100%) was obtained from Pharmco. THF was freshly distilled (sodium, benzophenone) prior to use. All metals were of 99.99% or greater purity. Silicon <100> wafers (p-doped, test grade) were obtained from Silicon Quest International.

**Preparation of Evaporated Metal Substrates.** All metal substrates were prepared by e-beam evaporation with a base pressure of ~1 x $10^{-7}$ Torr on test grade <100> silicon wafers with a typical evaporation rate of 2 Å/s. A titanium adhesion layer (2 nm) was applied to all substrates prior to deposition of 100 nm of the metal. All substrates were used within 20 min after removal from the vacuum chamber.

**Preparation of Template-Stripped Gold.** Template-stripped gold substrates were prepared as described previously.[14,15] A bare silicon substrate (<100>, p-doped, test grade) was treated with Piranha solution for 10 min. Gold was thermally evaporated at

a base pressure of 1 x $10^{-6}$. The initial evaporation rate was at 0.5 Å/s for the first 15 nm and then increased to 1.5 Å/s until a final thickness of between 100-150 nm was reached. The samples were cooled, removed from the chamber and attached to glass slides with EPO-TEK 377. Gold substrates were removed from their silicon backing as needed.

**Assembly Preparation**. Assemblies were performed with 1 mM solutions on freshly prepared substrates and an assembly time of 20-48 h. After assembly the samples were rinsed with the same solvent used for assembly, optionally sonicated in the case of the aromatic species, and dried under a stream of nitrogen. Platinum and silver assemblies were prepared in the drybox within 5 min after their removal from the evaporation chamber. As a control, gold samples were also assembled under drybox conditions. The compounds used for assembly are listed in Table 1.

**Water Contact Angle Measurements**. Contact angle measurements were performed using a Ramé-Hart goniometer model 100. Measurements were taken on at least two locations with at least five advancements of the drop of deionized water. Values shown are the average of at least two samples.

**Ellipsometric Measurements.** Measurements of surface optical constants and molecular layer thicknesses were taken with a single wavelength (632.8 nm laser) LSE Stokes Ellipsometer (Gaertner Scientific). The surface thickness was modeled as a single absorbing layer atop an infinitely thick substrate (fixed $n_s$). The observed error in repeated measurements of the same spot was typically 0.2 nm or less. The index of refraction was set at 1.45 for aliphatic assemblies and 1.55 for aromatic compounds.

**Infrared Reflection Spectroscopy Measurements.** A Nicolet Nexus 670 spectrometer with KBr beam splitter and MCT/A detector was used in conjunction with a SMART/SAGA grazing angle accessory, using a 16 mm diameter sampling area with p-polarized light fixed at an 80° angle of incidence.

**X-ray Photoelectron Spectroscopy (XPS) Measurements.** A PHI Quantera SXM XPS/ESCA system at 5 × $10^{-9}$ Torr was used to take photoelectron spectra. A monochromatic Al X-ray source at 100 W was used with an analytical spot size of 0.15 mm x 1.4 mm and a 45° takeoff angle, with pass energy of 26.00 eV. High resolution spectra of S 2p region used a 45° takeoff angle and 13.00 eV pass energy. Unless noted surface samples were referenced against internal Au $4f_{7/2}$ line at 84.0 eV, Ag $3d_{5/2}$ at 368.3 eV, or Pt $4f_{7/2}$ 71.2. Powder XPS photoelectron lines were referenced against C 1s signal at 284.50 eV.

| Number | Structure |
|---|---|
| 1 |   |
| 2 |   |
| 3 | 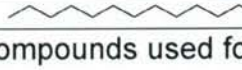  |

**Table 1.** Compounds used for assembly on precious metal surfaces.

**Results**

***Thiocyanates on Gold.*** Of all the metals, gold is the only substrate where thiocyanate assembly has been demonstrated.[1] It is known that thiocyanates react with gold to give the same thiolate bound monolayer as produced when starting with the free thiol. In the initial communication it was reported that the transient species $(CN)_{ads}$ was observed in a few cases. This observation warrants further analysis.

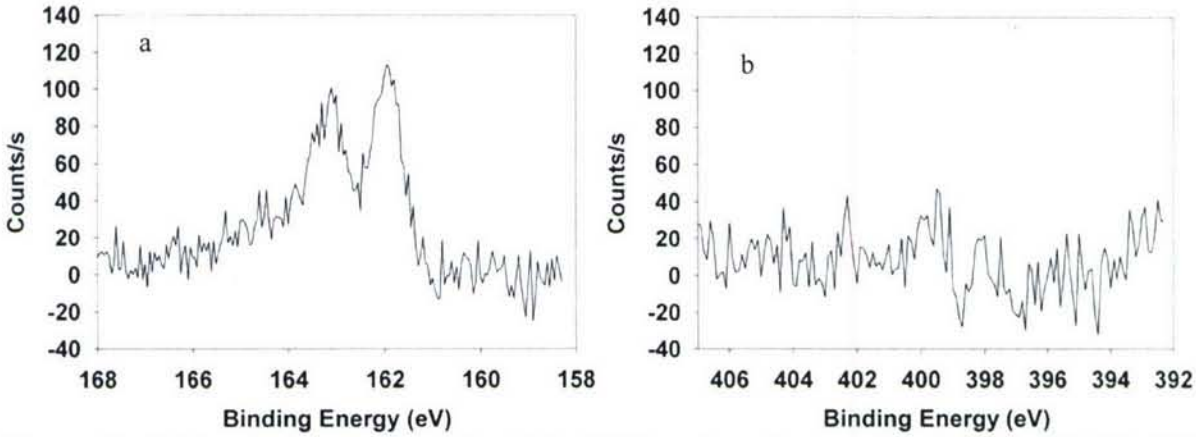


**Figure 2**. (a) Lack of a signal in the N 1s XPS region of assembled **1** on gold. (b) S 2p XPS region of assembled **1** on gold.

The analysis of a large number of assemblies shows a number of samples that contain no surface nitrogen (as seen by the N 1s signal in XPS) as well as a number of incomplete assemblies that do contain some nitrogen signal. The upper limit of assembly quality can be seen in Figures 2a and b where the signal to noise (acquired over 12 h) show that if any nitrogen signal is present, it is less than 5% relative to the sulfur signal. For all cases where nitrogen was seen, the relative atomic concentration of nitrogen versus sulfur on the surface can be used as a rough indication of the number of surface sites ($(\sqrt{3}x\sqrt{3})R30°$ for aliphatics, $(2\sqrt{3}x\sqrt{3})R30°$ for aromatics, Figures 3a-f)[16,17] occupied by those two elements. Contact angle and ellipsometry clearly support this assumption for the aliphatic species. Experiments with mixed disulfide monolayers (R-S-S-R′, where R and R′ are shown to be present on the surface in equal amounts but where R′ has minimal height) show that ellipsometry, and to a lesser extent contact angles, can be used as a rough indication of coverage by the longer species.[18]

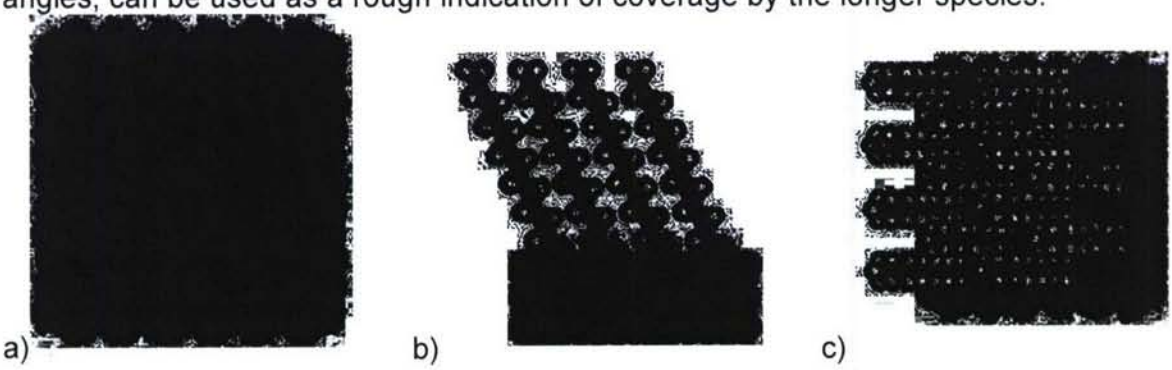

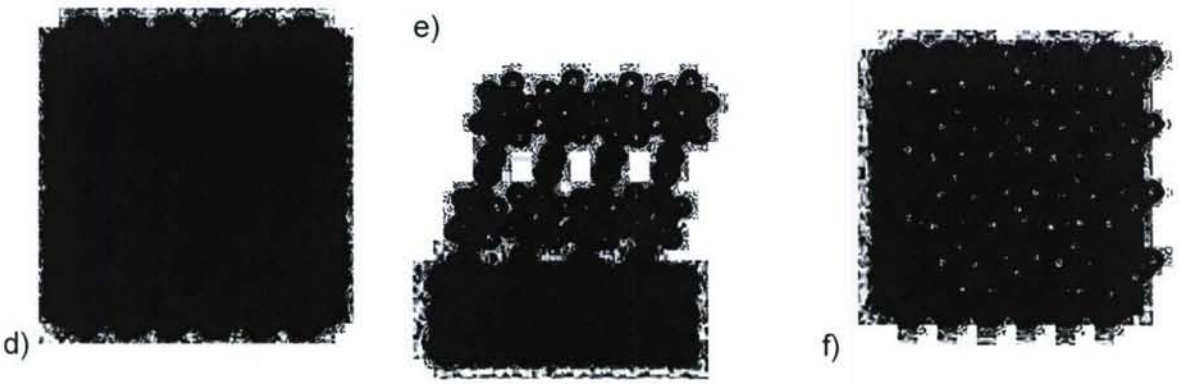


**Figure 3.** Packing structures of thiols on gold (111). (a) ($\sqrt{3}x\sqrt{3}$)R30° sulfur structure on a gold (111) surface. (b) the same lattice with a dodecane thiolate species. (c) A top view of b. (d) ($2\sqrt{3}x\sqrt{3}$)R30° sulfur structure for aromatic assemblies. The blue spots represent aromatic species that are rotated 90° with respect to the red species in the herringbone structure.[17] (e) the same lattice with a short conjugated ring system. (f) a top view of e.

Comparison of the these ellipsometric and contact values for organic thiocyanates to thiol controls show a difference in properties commensurate for a monolayer where a certain portion of the ($\sqrt{3}x\sqrt{3}$) sites (roughly equal to the N to S ratio) have been occupied by $Au(CN)_{ads}$ in the thiocyanate assemblies. This is shown in Table 2 where both the thickness and contact angles are significantly lower than that that of their thiol counterparts. In the case of the aromatic species the contact angle and ellipsometry measurements for the thiol and thiocyanates are nearly identical, suggesting that if CN is adsorbed on the surface the majority of this species is incorporated into other sites on the surface rather than replacing sulfur in the ($2\sqrt{3}x\sqrt{3}$)R30° lattice. Cyclic voltammetry studies[1] of the monolayers support this finding, though this cannot be used quantitatively.

| Molecule | Measured ellipsometric thickness (Å) | | Contact angle (°, static) | |
|---|---|---|---|---|
| | X=SH | X=SCN | X=SH | X=SCN |
| $nC_{12}H_{25}$-X | 16.4 | 12.2 | 105 | 97 |
| 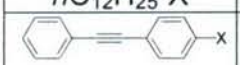 | 14.6 | 13.8 | 80 | 78 |

**Table 2.** Film thickness (±10%) determined by single wavelength ellipsometry and contact angle (±5%) (water) measurements.

The residual $Au(CN)_{ads}$ is seen both by infrared spectroscopy and XPS. An infrared signal is seen at 2160 $cm^{-1}$ (Figure 4a). A corresponding XPS signal is seen at 399.5 eV (Figure 4b). A second XPS N1s peak is seen with smaller frequency and intensity and occurs at 397.9 eV (Figure 4c). A corresponding infrared frequency has

not been established. Further explanation on the nature of these species can be found in the discussion section. These signals can be seen in both the aliphatic and aromatic thiocyanate assemblies.

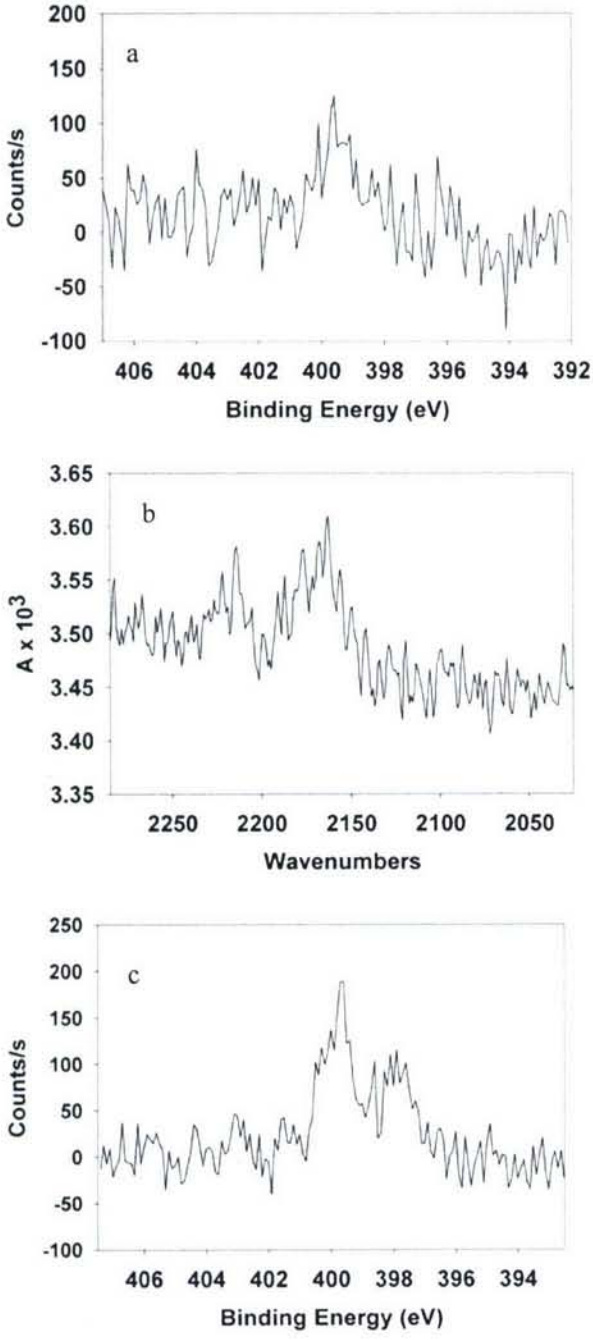


**Figure 4.** (a) Infrared reflection spectrum of assembled **2** on gold. Peak is located at 2160 $cm^{-1}$ (b) N 1s XPS region of assembled **3** on gold. (c) N

1s XPS region of assembled **2** on gold.

Some $(CN)_{ads}$ is detectable in the majority of the assemblies (for both aromatic and aliphatic thiocyanates). On evaporated gold the average over 12 identically prepared samples was 21% nitrogen on the surface (Figure 5) with a maximum of 37% and a minimum (2 samples) of no detected signal. This nitrogen signal was not seen in any of the thiol controls run side by side with thiocyanate assemblies.

The variance in nitrogen content between samples prepared from the same substrate is minimal (±3%), but samples from different gold substrates showed a large deviation. Side by side comparisons of samples prepared with varied assembly time, thiocyanate concentration, substrate size, and chain length all show no variance in the relative concentration of nitrogen on the surface, suggesting that it is the variation of the surface morphology between substrates that determines the amount of nitrogen on the surface, and not other experimental conditions.

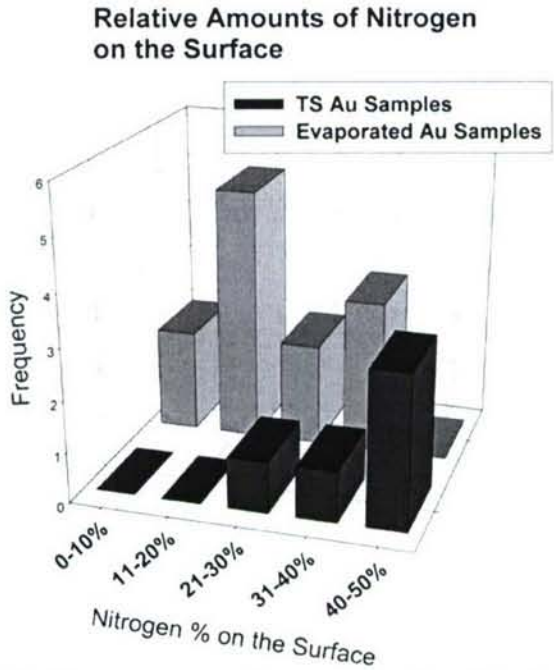


**Figure 5.** Occurrences of amounts of residual nitrogen for assemblies by XPS. Typical measurement errors are ± 3%. TS = template stripped.

The assemblies were examined on template stripped (TS) gold in order to reduce the amount of variance in the substrate between experiments. TS gold gives an extremely flat surface and allows for practically unlimited storage time since the surface is protected from atmospheric contaminants and roughening.[14,15] With this system tens of "identical" substrates can be produced and used over a period of weeks.

The TS gold showed substantially higher residual nitrogen (39% nitrogen average) compared to the evaporated gold. It also showed a smaller standard deviation

(7% nitrogen vs. 11% for the evaporated gold). We attribute the higher nitrogen count to the morphology of the surface much in the way edges and defect sites play a decisive role in thiolate assemblies.[19] This also supports our previous assertion regarding the dependence of the concentration of surface nitrogen on substrate surface morphology, since the surface morphology of evaporated gold is expected to vary from evaporation to evaporation.

***Thiocyanates on Silver.*** Thiolate assemblies on silver share surprisingly few features with their gold counterparts though both pristine surfaces have similarities. For example both the Au(111) and Ag(111) have nearly identical nearest-neighbor distances (2.88 and 2.89 Å, respectively)[16] and are readily etched by cyanide solutions.[20,21] However the thiolate monolayers have drastically different properties. Thiolates on silver have free energies of adsorption 45% more favorable than their counterparts on gold (1,2-benzenedithiol).[22] This stability is increased in the case of aliphatic chains by the greater packing density[6,9] and thus larger van der Waals forces. There is also a smaller variation in energy in the surface.[8] As a result of this packing arrangement, Ag(111) monolayers adopt a much smaller tilt angle (13° for Ag(111) vs. 26° for Au(111)).[11,13,23] The stronger chemisorption can also be seen in competitive displacement or desorption of the thiolates, where the rate constant on silver is an order of magnitude smaller than that of gold.[24] In Au(111), the energy difference between peak and valley is 6.0 kcal/mol vs. 3.3 kcal/mol for Ag(111).[8] Lastly, silver has a lower ionization energy (1.7 eV lower) and work function (0.6 eV)[6] and the metal-metal bond strength is weaker than that in gold.

Due to the much stronger lattice energy and higher packing density we assumed that the $Ag(CN)_{ads}$ signal would be present in all samples. However, just as in the case of gold, samples containing no significant amount of $Ag(CN)_{ads}$ were found (Figure 6a). As in the case of the gold sample, the sulfur 2p signal for the thiocyanates on silver (161.7, 162.9 eV) can be overlaid with that of free thiol assembly on the same substrate (161.8, 163.0 eV) (Figure 6b). If the expulsion of the M(CN) adsorbate was not dominated by the surface morphology we would expect to see a larger and more frequent appearance of $Ag(CN)_{ads}$ on the surface due to the increased intermolecular interaction of the monolayer. In some cases a $(CN)_{ads}$ XPS signal was seen at 399.4 eV (N 1s).

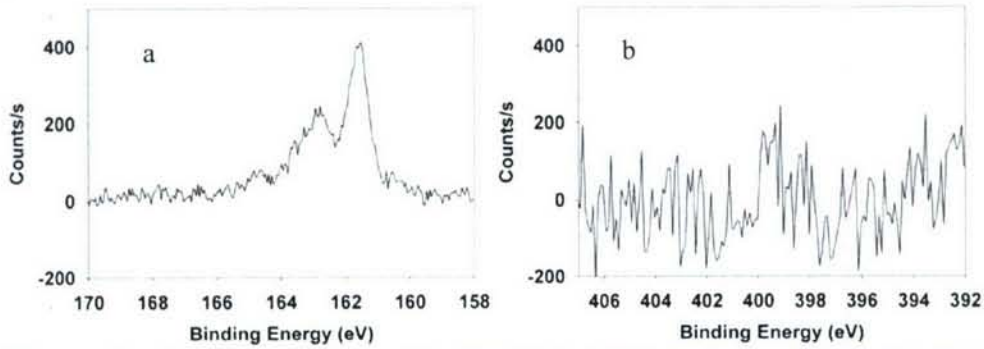


**Figure 6.** (a) Lack of signal in the N 1s XPS region of assembled **1** on silver. The spectrum has been referenced to the C 1s signal at 284.5 eV. (b) S 2p XPS region of assembled **1** on silver. The spectrum has been

referenced to the C 1s signal at 284.5 eV.

***Thiocyanates on Platinum***. Platinum provides another comparative substrate for the thiocyanate assembly. As opposed to gold and silver, which are easily etched by cyanide, platinum is robust to such treatment.[20] Since the initially proposed mechanism invokes the loss of $[Au(CN)_2]^-$ (for gold assemblies), examination of platinum assemblies may provide further evidence for or against this mechanism. Furthermore, platinum is an excellent reference since the adsorption of cyanide and cyanogen ($(CN)_2$) on platinum has been studied extensively[25-41] due the role of $(CN)_{ads}$ in the Andrussow synthesis of HCN.[42] In the case of cyanogen adsorption on platinum, three distinct entities are seen. The first is a non-dissociative adsorption of cyanogen ($\alpha$), the second is dissociated island CN ($\beta_1$) and the third is isolated dissociated CN ($\beta_2$).[28]

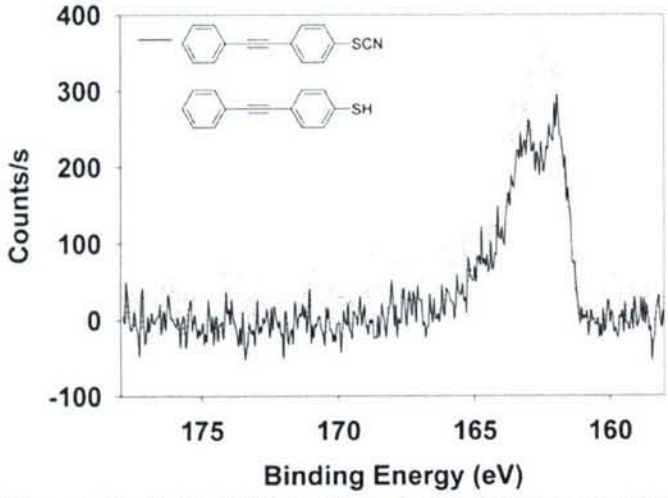


**Figure 7**. S 2p XPS region of assemblies on platinum.

As seen on other metals, the thiocyanate assemblies on platinum gave sulfur 2p signals (162.1, 163.3 eV) that are similar to their thiol counterparts (162.2, 163.4 eV) (Figure 7) indicating a carbon-sulfur bond cleavage and a thiolate bonding mechanism. The same residual nitrogen is seen in the platinum assemblies at 399.5 eV. It is also somewhat surprising that the ratio of sulfur to nitrogen on the surface is not 1:1; values as high as 4:1 are seen (Figure 8). The implications of this will be discussed in more detail below.

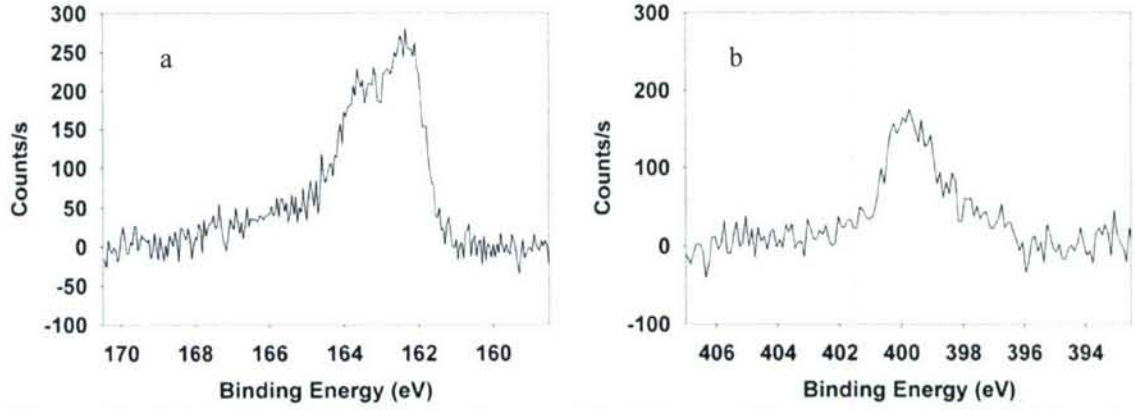


**Figure 8.** (a) S 2p XPS region of assembled **1** on platinum. (b) N 1s XPS region of assembled **1** on platinum.

## Discussion

***Nature of the N1s species.*** By XPS analysis, two types of residual nitrogen are seen in thiocyanate assemblies on all metals. Assignment of the peak at 397.7 eV on platinum (397.9 eV on gold), is made by comparing it to the well-studied adsorption of cyanide and cyanogen on platinum.[25-41] In the case of cyanogen adsorption on platinum, three distinct entities are seen. The first is a non-dissociative adsorption of cyanogen ($\alpha$), the second is dissociated "island" CN ($\beta_1$) and the third is "isolated" dissociated CN ($\beta_2$).[28] The "island" vs "isolated" cyanide show a large difference in reactivity.[26] The common adsorbed states $\alpha$, $\beta_1$, and $\beta_2$ have their respective binding energies at 397.7, 398.0, and 397.0 eV. Adsorptions studies of HCN on platinum support these previous studies with $(CN)_{ads}$ signal assigned to the 396.9 eV[25] and 397.0 eV.[32] Levoguer and Mills[32] also correlate their signal with an infrared frequency of 2078 $cm^{-1}$ for $(CN)_{ads}$ parallel to the surface normal. Similar frequencies are seen for the dissociative adsorption of $CH_3CN$.[33,34] This data is consistent with studies of $CN^-$ adsorption onto platinum electrodes which result in the same $(CN)_{ads}$ state.[30,31,35] The stable configuration for this is "on-top" binding with the cyanide oriented parallel to the surface normal.[27,36]

All of these comparisons indicate that the $M(CN)_{ads}$ we observe at 397.9/397.7 eV is clearly not on-top bonded CN ($\beta_2$). A more reasonable assignment is to a state similar to the $\beta_1$ state (island CN). The electron density on nitrogen (as seen by binding energy) is lower than seen in the on-top binding, indicating a more electron-poor nitrogen species. To reach this lower density, the $(CN)_{ads}$ must have a higher amount of $\pi$-back bonding to the metal atom.[36,37] This results in a weakened CN bond, which is often seen when the moiety occupies a hollow site or bridging configuration. However we cannot rule out that the constrained environment of the monolayer is forcing the cyanide into an atypical bonding mechanism. From the data, it is clear that whatever the configuration is, this species can be identified as cyanide bound to the metal surface.

The $(CN)_{ads}$ on the surface is clearly independent of the thiol moiety as observed by a change in the binding energy of the sulfur of the thiocyanate. Aromatic thiocyanates typically have a binding energy of 164.8 eV and 166.0 eV corresponding to

the S $2p^{3/2}$ and S $2p^{1/2}$ signals. Assemblies of these species show a dramatic shift in the binding energy corresponding to a large increase of electron density on the sulfur (162.0 eV and 163.3 eV).[1] This binding energy is identical to that seen in analogous free thiol assemblies and indicates that the sulfur ends up in the same thiolate species as when starting with the free thiol (Figure 9).[1] The presence of $CN_{ads}$ indicates that this is a surface-mediated reaction rather than a solution phase decomposition of the thiocyanate.

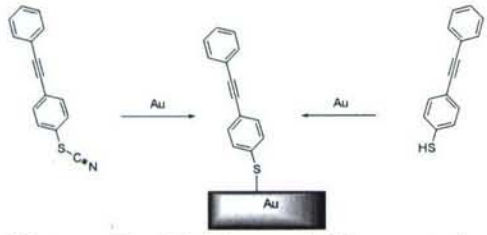


**Figure 9.** Thiols and thiocyanates give the same thiolate bonded molecule on the surface.

The second nitrogen species is distinguished by the infrared peak at 2160 $cm^{-1}$ and the XPS signal at 399.5 eV and has implications on the mechanism of $(CN)_{ads}$ displacement off the surface. This species has a stretching frequency substantially higher than any of the $(CN)_{ads}$ species on gold[4,5] or platinum[30,31,33,35] and is even higher than the frequency of $[Au(CN)_2]^-$ or $[Pt(CN)_4]^{2-}$.[39,40] This species is well known for platinum[31,35,41,43] (as well as palladium[29]) and does not come from $(CN)_{ads}$ but rather from the intermediate in the formation of $[Pt(CN)_4]^{2-}$. It was reported previously that infrared adsorption of this intermediate appears at 2160 $cm^{-1}$ at 0.1 V[33] (moving to lower wavenumbers at higher potentials) and is tentatively assigned to $[Pt(CN)_2]^{2-}$.[31,43] Au(CN) adsorbed on the gold surface shares a similar frequency (2160 $cm^{-1}$) with its platinum counterparts, suggesting that this is the nature of our second cyanide species on gold.[3] XPS lends further support to this assignment. As mentioned earlier, the electron density (as seen by the N 1s binding energy) is too high (399.5 eV) for CN adsorbed onto the surface. The binding energy is very close to the species at 399.3 eV as seen for $K_2Pt(CN)_4$[44] and indicates that cyanide state is much closer to the leached metal species than the linearly adsorbed state. The possibility that molecules bonded to the surface through the nitrogen lone pair could give this same XPS signal[34,45] can be discounted due to the lack of a R-S-CN sulfur signal in the XPS spectra (see Supporting Information). We have observed this signal and the signal at 397.7 eV when pristine gold is exposed to a solution of $KCN_{aq}$ and then thoroughly rinsed.

The spectroscopic evidence supports a mechanism for $(CN)_{ads}$ expulsion from the surface as $M(CN)_x$. Other mechanisms for the expulsion of $(CN)_{ads}$ are unlikely. The expulsion of $(CN)_{ads}$ as CN is unlikely since CN is an unstable radical species. The relative bond strengths of Au-S, Au-Au, and Au-CN are approximately 40, 53, and 90 kcal/mol respectively,[16,46,47] also making expulsion of CN unfavorable. The same bond strength argument applies to expulsion of $CN^-$. The only other option, without $M(CN)_x$ loss, is the expulsion of cyanogen. Temperature programmed desorption (TPD) experiments, however, show that a temperature of ~370 K is required to desorb

molecular cyanogen and ~750 K is required for the removal of dissociated cyanogen off of a surface.[25] Furthermore, we have seen that assemblies in non-polar solvents such as hexanes result in lower thicknesses and contact angles than those done in polar solvents such as methanol and THF. In this light, the removal of $[Au(CN)_2]^-$, $[Ag(CN)_2]^-$, and $[Pt(CN)_4]^{2-}$ is a more plausible mechanism.

A brief discussion of the loss of the metal cyanide anion is warranted. First observation suggests this is problematic as such salts are classically "insoluble" in organic solutions. However, the amount of charge dispersed in the solution is minimal, on the order of ~$10^{-8}$ M. This is less than what is seen in the classical electrochemical cell without a salt bridge. The classical rules of "ionic species are insoluble in organic solutions" also fail as classical "insoluble" salts (i.e. AgCl, $K_{sp}=10^{-10}$ $H_2O$) are soluble within the range that we claim. Also, even in freshly distilled organic solutions (as used for these assemblies), there are extraneous counter ions available at these levels. Due to the extreme difficulty in directly observing this species, the nature or presence of a counter ion will likely remain unknown.

$Pt + 4\ CN^- \rightarrow Pt(CN)_4^{2-} + e^-$ $\qquad$ $Au + 2\ CN^- \rightarrow Au(CN)_2^- + e^-$

$O_2 + 2\ H_2O + 4e^- \rightarrow 4\ OH^-$ $\qquad$ $O_2 + 2\ H_2O + 4e^- \rightarrow 4\ OH^-$

**Figure 10.** Electrochemical reactions responsible for the etching of platinum and gold by cyanide.

Further justification for the cyanide leaching mechanism is required since it is accepted that platinum does not undergo etching by $CN^-$ under standard conditions.[20] Yet we clearly see ratios of greater than 1:1 S to N on the surface (i.e. 4:1). Platinum is not etched by basic cyanide solutions due to the unfavorable oxidation of Pt to $Pt^{2+}$ at no applied bias.[48] At applied positive voltages the reaction proceeds as seen in Figure 10. The oxidation of gold is more favorable and the reaction proceeds even at negative potentials. In our system the platinum must donate an electron for each cyanide adsorbed on the surface, thus this problem is mitigated (Figure 11).

Finally, surface roughening due to the presence of –CN was minimal as determined by AFM comparison of the assembly of **1** to the **4**-assembled surface. The addition of KCN to the assembly mixture did not enhance the rate of assembly, but it did cause slow etching of the surface to occur.

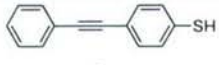


**4**

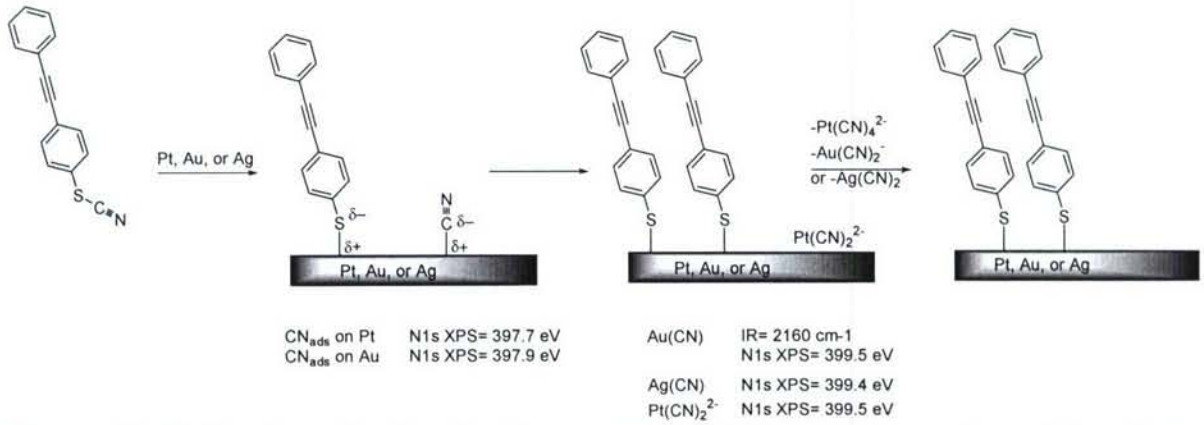


**Figure 11.** Refined mechanism for the assembly of thiocyanates onto metal surfaces based on XPS analysis of the surfaces.

## Summary

In this work we have demonstrated that the assembly mechanism for thiocyanates assembling on metal is similar for cases where the metal is platinum, silver and gold. In these cases the S-CN bond is cleaved leaving a species identical to that seen in free thiol assembly (Figure 11). In most cases a small amount of nitrogen residue is often found on the surface. This nitrogen manifests itself as one of two species, the first of which is cyanide adsorbed on the metal surface (N1s signal at 397.7 eV for Pt and 397.9 eV on Au). The second species (N1s signal at 399.4-399.5 eV) is identical to intermediate species often seen during the etching of metal surface by cyanide: $Pt(CN)_2^{2-}$ and AuCN (Figure 11). For gold the residual nitrogen appears an average of one time on the surface for every four sulfurs bound to the surface. Contact angle measurements and ellipsometry suggest, in the case of the aliphatic species, that the adsorbed CN prevents complete coverage of thiolates on the surface. In the case of the aromatic species, the data suggest the adsorbed cyanide is partially incorporated in the monolayer and interferes with thiolate adsorption to a smaller degree. Lastly, comparison of results on evaporated gold and silver to those on TS gold allows us to suggest that surface morphology plays a major role in the expulsion of cyanide from the surface.

## REFERENCES

(1) Ciszek, J. W.; Stewart, M. P.; Tour, J. M. *J. Am. Chem. Soc.* **2004**, *126*, 13172-13173.

(2) Han, P.; Sykes, E. C. H.; Pearl, T. P.; Weiss, P. S. *J. Phys. Chem. A* **2003**, *107*, 8124-8129.

(3) Yamada, T.; Sekine, R.; Sawaguchi, T. *J. Chem. Phys.* **2000**, *113*, 1217-1227.

(4) Gao, P.; Weaver, M. J. *J. Phys. Chem.* **1989**, *93*, 6205-6211.

(5) Kunimatsu, K.; Seki, H.; Golden, W. G.; Gordon, J. G. I.; Philpott, M. R. *Langmuir* **1988**, *4*, 337-341.

(6) Dhirani, A.; Hines, M. A.; Fisher, A. J.; Ismail, O.; Guyot-Sionnest, P. *Langmuir* **1995**, *11*, 2609-2614.
(7) Skriver, H. L.; Rosengaard, N. M. *Phys. Rev. B* **1992**, *46*, 7157-7168.
(8) Sellers, H.; A., U.; Shnidman, Y.; Eilers, J. E. *J. Am. Chem. Soc.* **1993**, *115*, 9389-9401.
(9) Fenter, P.; Eisenberger, P. *Langmuir* **1991**, *7*, 2013-2016.
(10) Li, Z. C., S.-C., Williams, S. R. *Langmuir* **2003**, *19*, 6744-6749.
(11) Walczak, M. M.; Chung, C.; Stole, S. m.; Widrig, C. A.; Porter, M. D. *J. Am. Chem. Soc.* **1991**, *113*, 2370-2378.
(12) Hatchett, D. W.; Uibel, R. H.; Stevenson, K. J.; Harris, J. M.; White, H. S. *J. Am. Chem. Soc.* **1998**, *120*, 1062-1069.
(13) Laibinis, P. E.; Whitesides, G. M.; Allara, D. L.; Tao, Y.-T.; Parikh, A. N.; Nuzzo, R. G. *J. Am. Chem. Soc.* **1991**, *113*, 7152-7167.
(14) Stamou, D.; Gourdon, D.; Leley, M.; Burnham, N. A.; Kulik, A.; Vogel, H.; Duschl, C. *Langmuir* **1997**, *13*, 2425-2428.
(15) Blackstock, J. J.; Li, Z.; Freeman, M. R.; Stewart, D. R. *Surf. Sci.* **2003**, *546*, 87-96.
(16) Ulman, A. *Chem. Rev.* **1996**, *96*, 1533-1554.
(17) Dhirani, A.-A.; W., Z. R.; Hsung, R. P.; Guyot-Sionnest, P.; Sita, L. R. *J. Am. Chem. Soc.* **1996**, *118*, 3319-3320.
(18) Biebuyck, H. A.; Whitesides, G. M. *Langmuir* **1993**, *9*, 1766-1770.
(19) Hostetler, M. J.; Templeton, A. C.; Murray, R. W. *Langmuir* **1999**, *15*, 3782-3789.
(20) Ammen, C. W. *Recovery and Refining of Precious Metals*; Chapman & Hall: New York, 1984.
(21) Gilchrist, J. D. *Extraction Metallurgy*; 3rd ed.; Pergamon Press: New York, 1989.
(22) Lee, Y. J.; Jeon, I. C.; Paik, W.; Kim, K. *Langmuir* **1996**, *12*, 5830-5837.
(23) Nuzzo, R. G.; Korenic, E. M.; Dubois, L. H. *J. Chem. Phys.* **1990**, *93*, 767-773.
(24) Schlenoff, J. B.; Li, M.; Ly, H. *J. Am. Chem. Soc.* **1995**, *117*, 12528-12536.
(25) Lindquist, J. M.; Ziegler, J. P.; Hemminger, J. C. *Surf. Sci.* **1989**, *210*, 27-45.
(26) Mills, P.; Jentz, D.; Trenary, M. *J. Am. Chem. Soc.* **1997**, *119*, 9002-9009.
(27) Ample, F.; Clotet, A.; Ricart, J. M. *Surf. Sci.* **2004**, *558*, 111-121.
(28) Hoffmann, W.; Bertel, E.; Netzer, F. P. *J. Catal.* **1979**, *60*, 316-324.
(29) Ashley, K.; Lazaga, M.; Samant, M. G.; Seki, H.; Philpott, M. R. *Surf. Sci.* **1989**, *219*, L590-L594.
(30) Stuhlmann, C. *Surf. Sci.* **1995**, *335*, 221-226.
(31) Kim, C. S.; Korzeniewski, C. *J. Phys. Chem.* **1993**, *97*, 9784-9787.
(32) Levoguer, C. V.; Nix, R. M. *J. Chem. Soc., Faraday Trans.* **1996**, *92*, 4799-4807.
(33) Dederichs, F.; Petukhova, A.; Daum, A. *J. Phys. Chem. B* **2001**, *105*, 5210-5216.
(34) Sexton, B.; Hughes, F. *Surf. Sci.* **1984**, *140*, 227-248.

(35) Stuhlmann, C.; Villegas, I.; Weaver, M. J. *Chem. Phys. Lett* **1994**, *219*, 319-324.
(36) Daum, W.; Dederichs, F.; Muller, J. E. *Phys. Rev. Lett.* **1998**, *80*, 766-769.
(37) Anderson, A. B.; Kotz, R.; Yeager, E. *Chem. Phys. Lett* **1981**, *82*, 130-134.
(38) Volmer, M.; Stratmann, M.; Viefhaus, H. *Surface and Interface Analysis* **1990**, *16*, 278-282.
(39) Kubas, G. J.; Jones, L. H. *Inorg. Chem.* **1974**, *13*, 2816-2819.
(40) Yau, J.; Mingos, M. P. *J. Chem. Soc., Dalton Trans.* **1997**, 1103-1111.
(41) Daum, W.; Friedrich, K. A.; Klunker, C.; Knabben, D.; Stimming, U.; H., I. *Appl. Phys. A* **1994**, *59*, 553-562.
(42) Satterfield, C. N. *Heterogeneous Catalysis in Practice*; McGraw-Hill: New York, 1980.
(43) Friedrich, K. A.; Daum, W.; Klunker, C.; Knabben, D.; Stimming, U.; Ibach, H. *Surf. Sci.* **1995**, *335*, 315-325.
(44) Hanks, T. W.; Ekeland, R. A.; Emerson, K.; Larsen, R. D.; Jennings, P. W. *Organometallics* **1987**, *6*, 28-32.
(45) Kishi, K.; Ikeda, S. *Surf. Sci.* **1981**, *107*, 405-416.
(46) Kordis, J.; Gingerich, K. A.; Seyse, R. J. *J. Chem. Phys.* **1974**, *61*, 5114-5121.
(47) Dietz, O.; Rayon, V. M.; Frenking, G. *Inorg. Chem.* **2003**, *42*, 4977-4984.
(48) Dorin, R.; Woods, R. *J. Appl. Electrochem.* **1991**, *21*, 419-424.